



**Cite this article:** Pietak A, Levin M. 2017

Bioelectric gene and reaction networks: computational modelling of genetic, biochemical and bioelectrical dynamics in pattern regulation. *J. R. Soc. Interface* **14**: 20170425.

<http://dx.doi.org/10.1098/rsif.2017.0425>

Received: 8 June 2017

Accepted: 31 August 2017

## Subject Category:

Life Sciences—Physics interface

## Subject Areas:

biophysics, computational biology, systems biology

## Keywords:

bioelectricity, regeneration, gene regulatory networks, *in silico* simulations

## Author for correspondence:

Michael Levin

e-mail: [michael.levin@tufts.edu](mailto:michael.levin@tufts.edu)

Electronic supplementary material is available online at <https://dx.doi.org/10.6084/m9.figshare.c.3878404>.

# Bioelectric gene and reaction networks: computational modelling of genetic, biochemical and bioelectrical dynamics in pattern regulation

Alexis Pietak and Michael Levin

Allen Discovery Center, Tufts University, Medford, MA, USA

ML, 0000-0001-7292-8084

Gene regulatory networks (GRNs) describe interactions between gene products and transcription factors that control gene expression. In combination with reaction–diffusion models, GRNs have enhanced comprehension of biological pattern formation. However, although it is well known that biological systems exploit an interplay of genetic and physical mechanisms, instructive factors such as transmembrane potential ( $V_{\text{mem}}$ ) have not been integrated into full GRN models. Here we extend regulatory networks to include bioelectric signalling, developing a novel synthesis: the bioelectricity-integrated gene and reaction (BIGR) network. Using *in silico* simulations, we highlight the capacity for  $V_{\text{mem}}$  to alter steady-state concentrations of key signalling molecules inside and out of cells. We characterize fundamental feedbacks where  $V_{\text{mem}}$  both controls, and is in turn regulated by, biochemical signals and thereby demonstrate  $V_{\text{mem}}$  homeostatic control,  $V_{\text{mem}}$  memory and  $V_{\text{mem}}$  controlled state switching. BIGR networks demonstrating hysteresis are identified as a mechanisms through which more complex patterns of stable  $V_{\text{mem}}$  spots and stripes, along with correlated concentration patterns, can spontaneously emerge. As further proof of principle, we present and analyse a BIGR network model that mechanistically explains key aspects of the remarkable regenerative powers of creatures such as planarian flatworms. The functional properties of BIGR networks generate the first testable, quantitative hypotheses for biophysical mechanisms underlying the stability and adaptive regulation of anatomical bioelectric pattern.

## 1. Introduction

Large-scale biological patterning in development, regeneration and disease remains among the most fundamental and important questions facing modern biology. Metazoan organisms reliably self-assemble a complex body plan from a single fertilized egg cell; furthermore, many animals, such as salamanders and planaria, are able to repair or remodel their bodies back to the correct shape despite injury and other types of drastic perturbation such as limb amputation [1,2]. Understanding the mechanisms that control the formation and regulation of organism-scale biological patterns may allow us to mitigate birth defects, implement organ regeneration strategies and to prevent, heal or even reprogramme the cancer state [3]. It is crucial to begin to understand and exploit the multicellular algorithms and dynamics that control anatomy and its remodelling, in addition to the details of subcellular signalling pathways.

Biological pattern formation is highly complex, involving numerous biomolecular mechanisms that lead to formation of instructive chemical patterns in a tissue collective, as well as mechanical considerations concerning shape changes and movements of individual cells and the tissue substratum as a whole. From the chemical patterning perspective pioneered by Turing [4] and Wolpert [5] (among others [6–8]), individual cells produce a variety of substances which may: (i) have the capacity to influence the production of other substances via genetic expression

or chemical reactions, (ii) travel through the cellular collective via diffusive transport, thereby generating patterns of spatial concentration, and (iii) ultimately lead to changes in the gene expression profile of a cell, thereby serving to establish cell identity and other subsequent cell behaviours. A core concept in chemical patterning is that of positional information [7,9], whereby the dynamics of the complete tissue system establish positional information as spatial patterns of an instructive signal, such as a concentration gradient of a morphogenic substance, which cells ‘interpret’ in order to determine their position in space and ‘decide’ on an outcome appropriate for generation of a specific final body plan.

Gene regulatory networks (GRNs) help supply mechanistic details to more precisely define how cells can interpret chemical signals, and how this in turn establishes cell fate outcomes. GRN models describe a collection of biomolecular agents that interact with one another in activation or inhibition relationships to ultimately control the expression profile of genes in a cell [10]. As a cell’s profile of genetic expression is a primary defining feature of the cell’s phenotype, GRNs maintain an effective description of cell status, with the ability to predict and determine cell fate under various circumstances. By assembling and synthesizing well-supported equations that describe physical processes such as diffusion, continuous mathematical models of GRN dynamics predict how gene regulatory substances diffuse through the cell network and represent one mechanism involved in the generation and evolution of biomolecular positional information as a function of time and space. Importantly, these models provide a clear and reasonable connection between the patterned concentration of a substance and the pattern of cell fate outcomes. Indeed, GRNs have been used to successfully describe aspects of pattern formation during morphogenesis [11–14] and regeneration [15]. However, published GRNs are commonly composed of (i) nodes that are exclusively gene products, RNAs, proteins or other regulators and (ii) edge relationships (connecting lines or arrows) describing activation or inhibition interactions between nodes. *In vivo*, however, other types of chemical reactions, particularly those of metabolism, are well known to affect gene expression and other factors influencing physiological status [6,16,17]. Therefore, a heterogeneous network structure involving gene and reaction products, as well as chemical reactions between nodes, can be defined [18]; this suggests an integration that bridges the gap between GRNs and reaction–diffusion (RD) schemes [7] and enables thinking in terms of general regulatory networks. Understanding the spatial dynamics of such networks in the context of establishing or remodelling complex anatomical structures, as well as integrating with the physics known to be involved in morphogenesis, is a key challenge for biomedicine as well as basic evolutionary developmental biology.

While chemical and mechanical perspectives greatly assist our understanding of biological patterning, a wide array of experimental studies performed over the last century have uncovered bioelectric signals (ion-flux dependent phenomena, such as trans-membrane potential ( $V_{\text{mem}}$ ) [19]) as another crucial instructive factor [20–25]. For example, it has long been known that application of external electric fields can switch the polarity of head/tail regeneration in planarian fragments [26,27] and hydra [25]. While classical data in this field used applied fields delivered via electrodes, the recent decade has seen the development of novel molecular tools for manipulating resting potential of cells *in vivo*. Techniques include

ion-channel gene misexpression and knockdown, optogenetics, and pharmacological reagents [28–32]. Endogenous bioelectric signalling ultimately arises from  $V_{\text{mem}}$ , an electrical property exhibited by all living cells, which has physiological outcomes from the scale of genetic expression to the development of whole organs [22,33,34]. In single cells,  $V_{\text{mem}}$  influences key behaviours such as the proliferation, migration and differentiation of somatic, stem and cancer cell state [35–37]. On the larger scale, networks of cells (of all types, not just neurons) communicate via endogenous dynamics of spatio-temporally distributed  $V_{\text{mem}}$  to form circuits that regulate organ-level patterning [38–41]. Endogenous bioelectric signalling has been shown to be involved in the regulation of brain size, appendage length, head shape and axial patterning of the entire body [33,42–47]. Moreover, experimental manipulation of endogenous  $V_{\text{mem}}$  gradients in *Xenopus* has induced the formation of complete eyes in posterior locations even including the gut [48], triggered regeneration of entire appendages including limbs and spinal cord [49,50], and normalized tumours [51,52]. Recent studies have identified the endogenous ion channels and pumps responsible for specific patterning functions of  $V_{\text{mem}}$ , and uncovered several mechanisms by which  $V_{\text{mem}}$  changes are transduced into second messenger cascades that initiate highly conserved transcriptional and chromatin changes downstream of bioelectric signalling [53].

The development of molecular-level tools for manipulating bioelectrical signalling and mechanistically tracking its intracellular targets is proceeding rapidly [33,54–56]; however, two main knowledge gaps face the field. First, there is little understanding of the large-scale spatio-temporal dynamics of somatic bioelectrical networks, and it remains largely unclear how developmental bioelectricity is involved in the storage and process of spatial information that guides the pattern homeostasis observed in regulative development and regeneration. Specifically, multicellular bioelectric circuits have the potential for complex and non-obvious behaviour making quantitative modelling essential in order to predict behaviour and rationally design intervention strategies that manipulate  $V_{\text{mem}}$  towards states that induce desired downstream changes in growth and form. Second, while it is widely recognized that a true picture of patterning must include both genetic and biophysical control systems, there has been no integration of GRN models with this important aspects of biophysics. For example, recent models of planarian regeneration have been proposed in terms of GRNs [57–61] or RD models [62,63] and evidence has been collected for an instructive patterning role of bioelectricity [38,42,64]; however, no models exist which integrate the known genetic and bioelectric data into a comprehensive picture.

Our work, therefore, seeks to overcome several main barriers to progress. We sought to provide, and illustrate the use of, a hybrid modelling environment allowing more realistic models to be formulated, which include both the genetics and the physiology. We describe here a substantial extension of our recent work in which we presented the first simulation environment for studying spatialized developmental bioelectricity [65]. Specifically, we examined the different ways that  $V_{\text{mem}}$  can interact with, and direct outcomes in, heterogeneous networks that blend conventional GRNs with bioelectric signals. We focus on mechanisms besides the obvious impact that general gene expression can have on the presence of proteinaceous ion pumps and channels in a cell—an interesting topic that has been recently modelled in a single gene– $V_{\text{mem}}$

interaction loop by Cervera *et al.* [66]. We began by examining the ways that  $V_{\text{mem}}$  can influence steady-state levels of important signalling molecules in cells. We then identified the specific functional network moieties involved by introducing  $V_{\text{mem}}$  signals to regulatory networks and examining their specific functions as meta-structures of regulatory networks, analogous to components of an electrical circuit board. Finally, we examined the potential influence of  $V_{\text{mem}}$  signals in a cell network by modelling sheets of cells coupled by the electrical synapses known as gap junctions (GJs), demonstrating how positional information profiles are fundamentally different when  $V_{\text{mem}}$  is considered. To effectively explore the role of  $V_{\text{mem}}$  in biological pattern control, we focus on two different kinds of network-based dynamic systems: (i) mixed regulatory signal networks, referred to as Bioelectricity-Integrated Gene and Reaction (BIGR) networks, which arise in single cells and wherein the network nodes may be a diverse array of entities such as the concentration of expressed gene products or enzymes (as in conventional GRNs), transmembrane voltage  $V_{\text{mem}}$ , or ion channel states and (ii) spatial networks comprised of coupled biological cells, wherein each cell internally supports a BIGR network. The nodes of the spatial network are cells and the intercellular coupling occurs via electrodiffusive transport of charged substances via GJs [67]. As proof of principle, we use a simple model of an axially regenerating animal (e.g. planaria) as a focus point to illustrate combined features of BIGR and cell networks, and to highlight unique roles of bioelectrical signalling in pattern formation and regulation. Importantly, it is not currently known what the functional capabilities of bioelectric signals are, especially when coupled with GRNs. This analysis of BIGR dynamics reveals for the first time key basic properties of such hybrid networks, facilitating their modelling via our new platform. Our goal is to lower the barrier for researchers working on pattern regulation to formulate testable, quantitative, generative models to explain developmental/regenerative data, and to help design strategies for biomedical and bioengineering contexts.

## 2. Material and methods

### 2.1. Bioelectric modelling

Bioelectrical modelling used the BioElectric Tissue Simulation Engine (BETSE), a finite-volume-based simulator specially designed to study bioelectrical dynamics [65]. In this work, we extend the BETSE simulator to incorporate user-defined regulatory networks that may include factors such as gene products, chemical reactions, ions (some of which, such as  $\text{Ca}^{2+}$ , may be key secondary messengers), ion pumps and transporters, and ion channels into an integrated dynamic system. BETSE software and associated documentation are available from <https://ase.tufts.edu/biology/labs/levin/resources/software.htm>

The core BETSE algorithm handles bioelectric signalling by calculating all components of ion flux across membrane segments of a cell, calculating divergence of net flux across membranes to update concentrations in cells, calculating ion currents and charge in terms of net flux and concentration of ions in cells, and determining  $V_{\text{mem}}$  in terms of ion current and charge. All simulations included the ions  $\text{Na}^+$ ,  $\text{K}^+$ ,  $\text{Ca}^{2+}$ ,  $\text{Cl}^-$ ,  $\text{HCO}_3^-$ ,  $\text{H}^+$ , and non-membrane permeable anionic proteins modelled as  $\text{P}^-$ . Concentrations of ions (and all BIGR network substances) were defined in both intracellular and extracellular regions, with initial concentrations in both regions supplied by the user. All cells of all multicellular models presented herein are coupled via GJs,

which connect adjacent membranes of all neighbouring cells. Details are described in [65], where other essential equations and updates are detailed below and details outlined in the electronic supplementary material, S1.

The fundamental elements and aspects of bioelectric phenomena are reviewed in figure 1. ATP-powered ion pumps such as the ubiquitous sodium–potassium adenosine triphosphatase ion pump ( $\text{Na}^+/\text{K}^+$ -ATPase), which moves  $3\text{Na}^+$  from cell to extracellular space and  $2\text{K}^+$  from extracellular space to the cytosol for each ATP molecule that is hydrolysed (figure 1a), are instrumental in creating electrochemical gradients of  $\text{Na}^+$  and  $\text{K}^+$  across the membrane. In most metazoan cell types, the  $\text{Na}^+$  electrochemical gradient created by  $\text{Na}^+/\text{K}^+$ -ATPase activity favours movement of  $\text{Na}^+$  into cells, and therefore, depolarization of  $V_{\text{mem}}$  with increased membrane permeability to  $\text{Na}^+$  ions ( $P_{\text{mem}}\text{Na}$ ), whereas the  $\text{K}^+$  electrochemical gradient favours movement of  $\text{K}^+$  out of cells, and therefore, hyperpolarization of  $V_{\text{mem}}$  with increased membrane permeability to  $\text{K}^+$  ions ( $P_{\text{mem}}\text{K}$ ).

Transmembrane voltage ( $V_{\text{mem}}$ ) ultimately arises from net ion charge density across the membrane, where the membrane acts as a capacitor (figure 1b).  $V_{\text{mem}}$  was calculated from an initial state of 0.0 and zero net charge in cells using the net ion current density across the membrane ( $J_{\text{mem}}$ ) in proportion to the patch capacitance of the membrane ( $C_{\text{mem}} = 0.05 \text{ F m}^{-2}$ ), via the simple expression relating the change in voltage across a capacitor to the current density:

$$\frac{dV_{\text{mem}}}{dt} = -\frac{1}{C_{\text{mem}}} J_{\text{mem}}. \quad (2.1)$$

The net current across the membrane,  $J_{\text{mem}}$ , was described by the sum of total transmembrane ion fluxes,  $\Phi_i^{\text{tot}}$ , for each ion,  $i$ :

$$J_{\text{mem}} = \sum_i F z_i \Phi_i^{\text{tot}}, \quad (2.2)$$

where  $F$  is Faraday's constant ( $96485 \text{ C mol}^{-1}$ ) and  $z_i$  is the charge of the ion.

In turn, the total transmembrane flux of an ion could have contributions from possible ion pump/transporter activity ( $\Phi_i^{\text{pump}}$ ), passive base transmembrane flux ( $\Phi_i^{\text{mem}}$ ), passive transmembrane flux from open ion channel presence ( $\Phi_i^{\text{chan}}$ ) or passive transport between GJ-coupled cells ( $\Phi_i^{\text{GJ}}$ ):

$$\Phi_i^{\text{tot}} = \Phi_i^{\text{pump}} + \Phi_i^{\text{mem}} + \Phi_i^{\text{chan}} + \Phi_i^{\text{GJ}}. \quad (2.3)$$

Passive base transmembrane flux of an ion,  $i$ , was calculated using the GHK flux equation:

$$\Phi_i^{\text{mem}} = \frac{z_i V_{\text{mem}} F P_i^{\text{mem}}}{RT} \left( \frac{c_i^{\text{cell}} - c_i^{\text{env}} \exp(-z_i V_{\text{mem}} F/RT)}{1 - \exp(-z_i V_{\text{mem}} F/RT)} \right), \quad (2.4)$$

where  $P_i^{\text{mem}}$  is the base permeability of the ion through the membrane,  $R = 8.3145 \text{ J mol}^{-1} \text{ K}$  is the ideal gas constant,  $T = 310 \text{ K}$  is the temperature,  $c_i^{\text{cell}}$  and  $c_i^{\text{env}}$  are the concentrations of the ion inside and outside of the cell, respectively.

Ion channels with open/closed states that are unregulated by chemical substances or  $V_{\text{mem}}$  are referred to as leak channels (figure 1c). Leak channels were modelled as supplying a component of transmembrane flux proportional to the effective permeability of the channel:

$$\Phi_i^{\text{chan}} = \frac{z_i V_{\text{mem}} F P_i^{\text{chan}}}{RT} \left( \frac{c_i^{\text{cell}} - c_i^{\text{env}} \exp(-z_i V_{\text{mem}} F/RT)}{1 - \exp(-z_i V_{\text{mem}} F/RT)} \right). \quad (2.5)$$

Ion channels with open/closed states regulated by chemical substances are referred to as ligand-gated channels (figure 1c), and were modelled by assuming the effective permeability of the channel ( $P_i^{\text{chan}}$ ) was modulated by the concentration of a gating ligand ( $cG$ ). For agonists, the general expression for



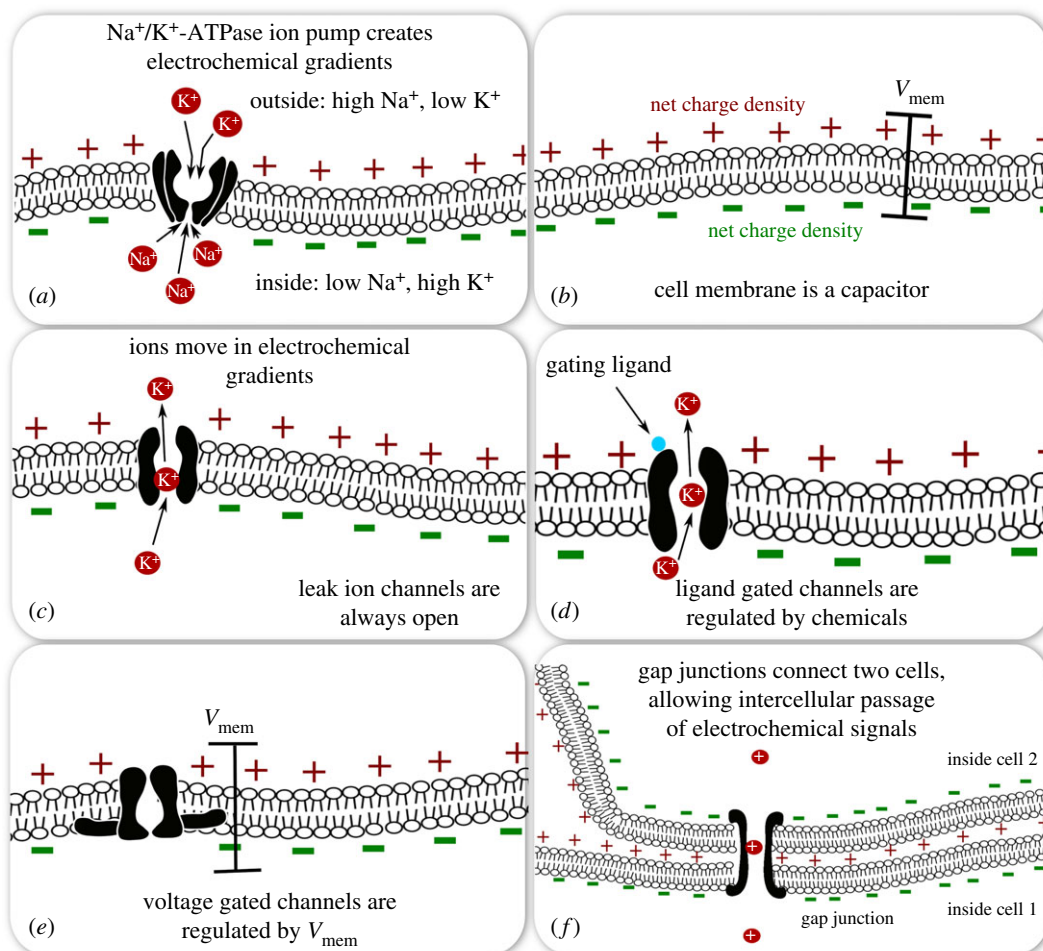


**Figure 1.** General overview of the basic functional units of bioelectricity. Ion pumps generate charge and concentration (i.e. electrochemical) gradients (a). Trans-membrane voltage ( $V_{\text{mem}}$ ) is generated by a net charge density at the inner and outer folds of the cell's plasma membrane, where the membrane acts as a capacitor,  $C_{\text{mem}}$  (b). Ion channels increase the membrane permeability to specific ions (c–f). Leak channels refer to channels that are generally always open, such as the K<sup>+</sup> channel KCNK9 (c). Chemically gated channels, such as the ATP-sensitive K<sup>+</sup> channel, open or close in response to the concentration of a gating ligand (d). Voltage-gated channels are sensitive to  $V_{\text{mem}}$  (e). Gap junctions connect the cytosol of two cells, allowing chemical and electrical signals to pass (f).

channel gating used was

$$p_i^{\text{chan}} = \frac{(cG/K_{1/2})^n}{1 + (cG/K_{1/2})^n}. \quad (2.6)$$

For antagonists, the expression used to modulate the channel permeability was

$$p_i^{\text{chan}} = \frac{1}{1 + (cG/K_{1/2})^n}. \quad (2.7)$$

Notably, cationic substances blocking ion channels have shown  $V_{\text{mem}}$ -sensitivity in their gating, due to changes in the intensity of channel pore blocking as a function of  $V_{\text{mem}}$ , which allows the channel state to be regulated by  $V_{\text{mem}}$  as well as the concentration of the gating ligand [68–74]. This voltage-sensitivity of ligand gating was modelled using a  $V_{\text{mem}}$ -dependent  $K_{1/2}$  value for the channel gating, as described in [68,74]. For example, a channel blocked in a voltage-sensitive manner by a substance with effective charge at the membrane of  $z_i^{\text{eff}}$ , and blocking the channel from the cytosolic side of the membrane, would have the  $K_{1/2}$  value for channel block described by

$$K_{1/2} = K_{1/2}^0 \exp\left(\frac{-V_{\text{mem}} z_i^{\text{eff}} F}{RT}\right). \quad (2.8)$$

A voltage-sensitive Mg<sup>2+</sup> block was used to model the behaviour of the Kir2.1 channel [68] and ATP-sensitive Kir

(ATP-Kir, Kir6.1 or Kir6.2) channel models [74], with further information given in the electronic supplementary material, S1.

Other ion channels with open/closed state that are altered by  $V_{\text{mem}}$  (figure 1e) use Hodgkin–Huxley differential equations to modulate the value of channel  $p_i^{\text{chan}}$  in response to  $V_{\text{mem}}$ . Here we use a model for the voltage sensitive calcium channel (Ca<sub>v</sub>1.2) developed by Avery *et al.* [75] and a model for a delayed-rectifier K<sub>v</sub>1.5 developed by Philipson *et al.* [76].

GJs are channels that bridge the cytoplasm of two cells, enabling the passage of chemical and electrical signals (figure 1f). Ion flux through GJs was modelled using the Nernst–Planck equation:

$$\Phi_i^{\text{gj}} = -\beta_{\text{gj}} D_i^{\text{gj}} \nabla c_{\text{gj}} - \frac{\beta_{\text{gj}} D_i^{\text{gj}} z_i q}{k_b T} c_i \nabla V_{\text{gj}}, \quad (2.9)$$

where  $\beta_{\text{gj}}$  is the voltage-sensitivity scaling parameter (modelled as described in [77]),  $D_i^{\text{gj}}$  is the effective diffusion constant of the ion through GJs,  $\nabla c_{\text{gj}}$  is the concentration gradient of the ion across the GJ,  $\nabla V_{\text{gj}}$  is the difference in  $V_{\text{mem}}$  across the two GJ coupled cells,  $q = 1.6 \times 10^{-19}$  C is the unit charge constant and  $k_b$  is Boltzmann's constant.

In general, the equilibrium or 'resting'  $V_{\text{mem}}$  can be estimated in terms of ion concentration and membrane permeabilities using the Goldman equation [78].

Transport of chemical substances in the extracellular spaces and global environment was similarly calculated using

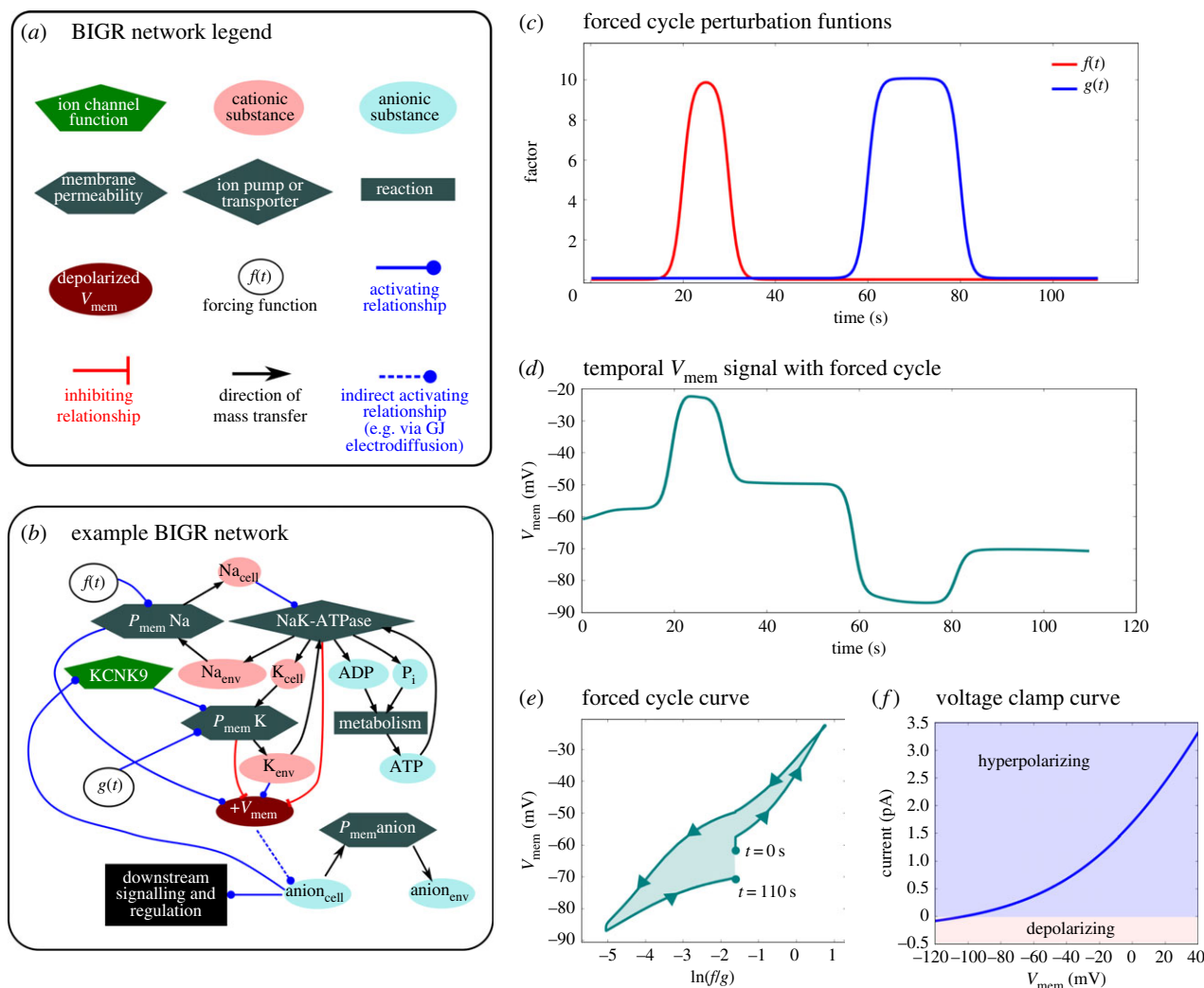


**Figure 2.** Basic terminology of BIGNET networks and a description of test simulations used to understand key characteristics of a BIGNET network. Different elements of a BIGNET network (a). An example of BIGNET network is shown in (b). To study properties of networks such as the one shown in (b), a ‘forced cycle’ test simulation was designed to create a transient perturbation to  $V_{\text{mem}}$  by multiplying base  $\text{Na}^+$  membrane permeability by the function  $10f(t)$ , and by multiplying the base membrane permeability to  $\text{K}^+$  ions by  $10g(t)$  (c). The application of the forced cycle simulation to a single cell running the BIGNET network shown in (b), generates a time-dependent change in resting  $V_{\text{mem}}$  of the form shown in (d). Plotting  $V_{\text{mem}}$  versus the natural logarithm of  $f(t)/g(t)$  generates a ‘forced cycle curve’ (e). The forced cycle curve depicts potential hysteresis of  $V_{\text{mem}}$  state via the area of the curve contained by forwards and backwards paths (shaded region of (e)). A separate ‘voltage clamp’ test was used to explore the activity of single channels in the context of a BIGNET network and to connect with standard electrophysiology measurements (f).

a standard diffusion equation, assuming zero voltage in the extracellular spaces:

$$\Phi_{\text{env}_i} = -D_i \nabla c_{\text{env}_i}. \quad (2.10)$$

The total change in concentration in a single cell from transmembrane passage was calculated by taking the divergence of all components of flux:

$$\frac{\partial c_{\text{cell}}^i}{\partial t} = -\nabla \cdot \Phi_{\text{tot}}^i. \quad (2.11)$$

## 2.2. Bioelectricity-integrated gene and reaction networks definition

We extended the BETSE platform described in [65] to include BIGNET network capabilities, where regulatory networks were automatically constructed by the software from user-specified input data using mathematical template equations to assemble differential equations describing activator/inhibitor relationships, rate equations for substance production and decay (simulating gene expression), rate equations for chemical reactions between substances of the network, and equations describing transmembrane

pump, transporter and ion channel flux. All substances in a BIGNET network model have concentration defined in both the intracellular space and the extracellular environment. Details regarding environmental handling of concentrations between the intra- and extracellular environments are described in [65].

Basic terminology of BIGNET networks and a description of test simulations used to understand key characteristics of a BIGNET network are detailed in figure 2. Different elements (e.g. ion channels, pumps, reactions) of a BIGNET network are denoted by node shapes of different form and colour, while the various relationships between elements (e.g. activation/inhibition) are indicated by directed line segments with different features (figure 2a). The following outlines the theory used to define general elements and relationships of BIGNET networks.

### 2.2.1. Activation and inhibition

BIGNET network models allowed the concentration of any substance to serve an activation or inhibition role over a model construct, where constructs may be: the growth rate of a gene product, the rate of an enzymatic reaction or transporter, the diffusion constant of an ion channel or the permeability of GJs. The activation/inhibition relationship was calculated in terms of a

scalar modulator coefficient. In all network diagrams shown herein, activators are indicated by blue lines with circular end-points, while inhibitors are shown as red lines with flat endings (figure 2b).

A general substance 'A' with a concentration-dependent activating effect on another element was modelled in terms of a modulating coefficient multiplied to the activity of the response element,  $\alpha_A$ , which was described by the Hill function:

$$\alpha_A = \frac{([A]/K_A)^{n_A}}{(1 + ([A]/K_A)^{n_A})}. \quad (2.12)$$

By contrast, an inhibiting effect was described in terms of a modulating coefficient  $\beta_A$  using the Hill function:

$$\beta_A = \frac{1}{(1 + ([A]/K_A)^{n_A})}. \quad (2.13)$$

### 2.2.2. Substance growth and decay

Basic growth and decay expressions were used to represent substances synthesized by cells (e.g. neurotransmitters, gene products, enzymes), when they are produced without a prescribed chemical reaction directly involving other nodes of the network—this is a typical feature of continuous GRN models [10]. In all network diagrams shown herein, nodes with a substance growth and decay relationship are indicated by a standard black arrow beginning and ending on the same node (figure 2b).

For example, a hypothetical substance with concentration  $[A]$  with growth inhibited by substance 'B', would have a rate of change described by

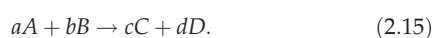
$$\frac{d[A]}{dt} = \beta_B r_A^{\max} - \delta_A [A], \quad (2.14)$$

where  $r_A^{\max}$  represents the maximum growth rate of 'A',  $\delta_A$  the maximum decay rate of 'A' and  $\beta_B$  the concentration-dependent growth-inhibition of 'A' by substance 'B', which would assume the form of equation (2.13).

### 2.2.3. Chemical reactions

Chemical reactions representing a mass conversion of network substances into other network substances were handled using rate equations based on fundamental chemical concepts, similar to those outlined in [79]. In all network diagrams shown herein, chemical reactions are indicated by rectangular boxes, where reagents/products flow into/out of the reaction box as indicated by standard black arrows (figure 2b).

As an example, for a hypothetical reaction:



The total reaction rate  $r_{\text{reaction}}$  is defined in terms of forward and reverse rate coefficients,  $r_f$  and  $r_r$ , respectively. An irreversible reaction defines  $r_{\text{reaction}}$  in terms of  $r_f$  as

$$r_{\text{reaction}} = r_f = r_{\max} \left( \frac{([A]/K_A)^a}{1 + ([A]/K_A)^a} \right) \left( \frac{([B]/K_B)^b}{1 + ([B]/K_B)^b} \right), \quad (2.16)$$

where  $K_A$  and  $K_B$  are constants defining the concentrations of  $[A]$  or  $[B]$  at which the reaction rate is half of its maximum value, and  $r_{\max}$  is a constant defining the maximum reaction rate.

For reversible reactions, a reaction quotient  $Q$  was defined as

$$Q = \frac{[C]^c [D]^d}{[A]^a [B]^b}, \quad (2.17)$$

where concentrations of substances in  $Q$  are in units of  $\text{mol l}^{-1}$ .

The equilibrium constant for the reaction was defined in terms of  $\Delta G^0$ , the standard free energy change for the reaction:

$$K_{\text{eqm}} = \exp\left(-\frac{\Delta G^0}{RT}\right). \quad (2.18)$$

The total reversible reaction rate was calculated in terms of both products and reactants with the balance between forward and reverse reaction rates decided by the ratio between  $Q$  and  $K_{\text{eqm}}$ . Using the simple example equation shown above, the reaction rate would be described

$$r_{\text{reaction}} = r_{\max} \left( r_f - \frac{Q}{K_{\text{eqm}}} r_r \right). \quad (2.19)$$

### 2.2.4. Transmembrane ion pumps and transporters

Transmembrane transporters were treated as reactions occurring across membranes, where ion pumps feature an additional chemical reaction (such as ATP hydrolysis) occurring in the cytosol. Ion transporters and pumps differ from chemical reactions as the equilibrium constant of the reaction was altered by the inclusion of new terms depending on the charge of the substances being transported across the membrane, and the magnitude of  $V_{\text{mem}}$ .

Transporter/pump reaction rate constants and reaction quotients were defined as described for cytosolic chemical reactions (equations (2.16) and (2.17)). The equilibrium constant for the general transporter/ion pump was also defined according to equation (2.18).

The definition for free energy change of a general chemical reaction was taken as [79]

$$\Delta G = \sum_{\text{prod}_i} a_i \mu_i - \sum_{\text{react}_j} a_j \mu_j. \quad (2.20)$$

However, instead of chemical potential, the *electrochemical* potential of each reactant or product was used, which assumed voltage to be zero outside of the cell, meaning the voltage inside the cell was equivalent to the value of  $V_{\text{mem}}$ :

$$\mu_i = \mu_o + z_i F V. \quad (2.21)$$

Electronic supplementary material, S1, describes models of the specific transporters: sodium–potassium adenosine triphosphatase ( $\text{Na}^+/\text{K}^+$ -ATPase) [80–83], sodium-dependent serotonin transporter (SERT) [84,85], organic cation transporter (OCT3) [86–89] and the divalent metal transporter (DMT1) [90–92], which are all presented herein. In all network diagrams, transporters are indicated by diamond-shaped boxes, where reagents/products flow into/out of the reaction box as indicated by standard black arrows (figure 2b).

### 2.2.5. Ion channels

Models of specific ion channels used in this work (KCNK9 and  $\text{K}^+$  channel [93],  $\text{Ca}_v1.2$  [75],  $\text{K}_v$  [76], Kir 2.1 [68] and ATP-Kir/Kir6.1/Kir6.2 [94,95]) are described in the electronic supplementary material, S1. In all network diagrams shown herein, ion channels are indicated by pentagon-shaped boxes (figure 2b).

### 2.2.6. pH handling

While not a focus of this introductory paper, our BETSE modelling system has the capability to model the transport of hydrogen ions and pH in the intra- and extracellular regions. The ability to create user-defined ion pumps, channels and chemical reactions (as described in the sections above) allows for the inclusion of  $\text{H}^+$  specific:

- ion pumps (e.g. the  $\text{H}^+/\text{K}^+$ -ATPase and plasma membrane V-ATPase ion pumps),
- ion channels (e.g. voltage-sensitive  $\text{H}^+$  channels),
- transporters (e.g. the MCT1 lactate/pyruvate transporter),
- a pH buffering reaction (e.g. the bicarbonate buffer), and
- the production of  $\text{H}^+$  via a chemical reaction (e.g. a metabolic production reaction).



Passive electrodiffusion of  $H^+$  across GJ, the plasma membrane and bulk regions of cytosol and the extracellular media is handled for any simulation that includes the  $H^+$  ion.

For the purposes of this introductory paper, we have chosen to focus on other ion channels, pumps and reactions, and therefore,  $H^+$  and pH are presently ignored.

## 2.3. Bioelectricity-integrated gene and reaction network investigation methods

### 2.3.1. Forced cycle perturbation analysis

To study the properties of BIGR networks such as the one shown in figure 2*b*, a 'forced cycle' test simulation was designed to create a transient perturbation inducing first a  $V_{\text{mem}}$  depolarization, and then a  $V_{\text{mem}}$  hyperpolarization, which finishes with the properties of the system identical to those at the beginning. The forced cycle test simulation uses two pulse functions,  $f(t)$  and  $g(t)$  of figure 2*c*, to induce a  $V_{\text{mem}}$  depolarization by transiently increasing the membrane permeability to  $Na^+$  ions by a factor of 10 by multiplying the base membrane permeability by  $f(t)$ , and to then induce a  $V_{\text{mem}}$  hyperpolarization by transiently increasing the membrane permeability to  $K^+$  ions by a factor of 10 by multiplying the base membrane permeability to  $K^+$  ions by  $g(t)$  (see implied role of  $f(t)$  and  $g(t)$  in BIGR network of figure 2*b*, and their temporal form in figure 2*c*). The application of the forced cycle simulation to a single cell running the BIGR network shown in figure 2*b* generates a time-dependent change in resting  $V_{\text{mem}}$  of the form shown in figure 2*d*. Plotting  $V_{\text{mem}}$  versus the natural logarithm of function  $f(t)/g(t)$  generates a 'forced cycle curve' (figure 2*e*). The forced cycle curve depicts any hysteresis of  $V_{\text{mem}}$  state via the area of the curve (shaded region of figure 2*e*), where area represents the degree to which forward and backward trajectories of the system differ from start ( $t = 0$  s) to end ( $t = 110$  s) of the transient perturbation cycle of functions  $f(t)$  and  $g(t)$  (figure 2*e*).

Ultimately, the two pulse functions  $f(t)$  and  $g(t)$  change  $V_{\text{mem}}$  by slowly and systematically altering the ratio of base membrane permeabilities to  $Na^+$  and  $K^+$  ( $P_{\text{mem}}^{Na} : P_{\text{mem}}^{K}$ ) as a function of time. We refer to the ratio  $P_{\text{mem}}^{Na} : P_{\text{mem}}^{K}$  as a control parameter, which *in vivo* or *in vitro* can be manipulated by modulating the open state of  $Na^+$  and  $K^+$  channels via a range of pharmacological or optogenetic interventions. This simulation format was chosen to enable visualization of hysteresis loops formed in systems that have memory capabilities, where the area of the hysteresis loop is an indication of the level of memory-forming capacity [96].

Forced cycle analysis was performed on single-cell simulations, where cells had a nominal diameter of 10  $\mu\text{m}$ .

### 2.3.2. Voltage clamp

'Voltage clamp' simulations were used to explore the steady-state activity of single channels in the context of a BIGR network, and to connect with electrophysiology measurements (figure 2*f*). Voltage clamp analyses were performed using single-cell simulations, where cells had a nominal diameter of 10  $\mu\text{m}$ . The voltage clamp curves shown in figure 2*f*, and the second column of figure 3, were created for different  $K^+$  channel models by fixing  $V_{\text{mem}}$  at a particular value in a range from  $-120$  mV to  $+40$  mV in 1 mV intervals for 2 s, and measuring the final current resulting from the  $K^+$  ion flux at the end of the 2 s hold period before advancing to the next  $V_{\text{mem}}$  value in the series. This 'voltage clamp' protocol was chosen to investigate the behaviour of the channel at steady state. For all voltage clamp curves, regions where current is above zero are shaded in blue and indicate where channel activity is hyperpolarizing of  $V_{\text{mem}}$ , whereas regions where current is below zero are shaded in red and indicate where channel activity is depolarizing of  $V_{\text{mem}}$ .

As shown in figure 3, the resulting  $I-V$  curves for the  $K^+$  leak channel model (based on a KCNK9 or TASK channel) reproduce the expected exponential form seen in experimental voltage clamp  $I-V$  curves for this channel class (fig. 2 of [97]). Likewise, the  $I-V$  curve for the inward-rectifier  $K^+$  channels and ATP-regulated inward-rectifier  $K^+$  channels (based on Kir2.1 and Kir6.1 channel types, respectively) reproduce the expected experimentally observed  $I-V$  curves commonly seen in the literature for the inward-rectifier channel class [98]. The  $I-V$  curve produced for our above-described voltage clamp simulation of the  $K_v1.5$  model does not correspond to experimental  $I-V$  curves reported in the literature (fig. 8 of [99]). However, we have determined that the voltage clamp protocol described above reproduces the steady-state  $I-V$  relation for the  $K_v1.5$  channel (as described in the electronic supplementary material, S1), and that when a voltage clamp protocol with a duty cycle, as described in McKay & Jennings [99], is simulated, which pulses between a hold voltage of  $-80$  mV to each voltage in the series and back to the hold voltage, measuring current at the pulsed voltage for 100 ms before returning to the hold voltage for 2 s, our simulator accurately reproduces experimentally observed  $I-V$  curves for the  $K_v1.5$  channel (see electronic supplementary material, S1).

## 2.4. Bioelectricity integrated anterior–posterior regeneration polarity control network

While there are many examples of  $V_{\text{mem}}$  involvement in pattern regulation, the planaria flatworm is an excellent model organism for the appreciation and investigation of bioelectric signalling, and its integration with genetic and biomolecular signalling networks. A central property of planaria and many other organisms is the ability to maintain and restore anatomical polarity and patterning along a major body axis. Indeed, the ability of earthworms to maintain axial patterning was investigated by T. H. Morgan as early as 1904, complete with emphasis placed on its bioelectric aspects [100]. After amputation of head and tail, the remaining portions of many worm species remember the previous orientation of head and tail, and each fragment of the worm regenerates the original head/tail orientation accordingly [101–104]. While much is known about the cellular mechanisms that are necessary for stem cell control during planaria regeneration, many unanswered questions remain about the mechanisms that ensure robust axial patterning. For instance, while chemical and genetic expression gradients are known to exist in planaria, and can explain the regeneration of head–tail at original locations in a central piece of the worm after amputation [59,105], it is much more difficult to describe how, at a single cut-line, two profoundly different outcomes will happen at the anterior and posterior edges of the same cut-line, where cells had the same positional information and yet go on to form radically different anatomical structures when surgically separated. Moreover, the pattern memory of planaria can be edited while maintaining a wild-type genome. For example, double-headed phenotypes can be induced by a range of manipulations, such as the application of an external voltage [26,27] or via a transient (i.e. 48 h) block of GJ permeability [43,106]. These perturbations induce permanent changes to the planarian body plan (the target morphology to which fragments regenerate), which are recapitulated in subsequent rounds of amputation and regeneration in plain water with no further manipulation [43].

In this work, we focus on a highly simplified case of regeneration of a planaria-like animal, as a case study into the role bioelectricity may play in axial patterning control.

Using simple and generic channels and substances, we constructed a BIGR network model (figure 4*a*) capable of spontaneously generating and regenerating chemical gradients along the long axis of an ellipse (taken to be the anterior–posterior axis of a flatworm), which furthermore demonstrates the expected

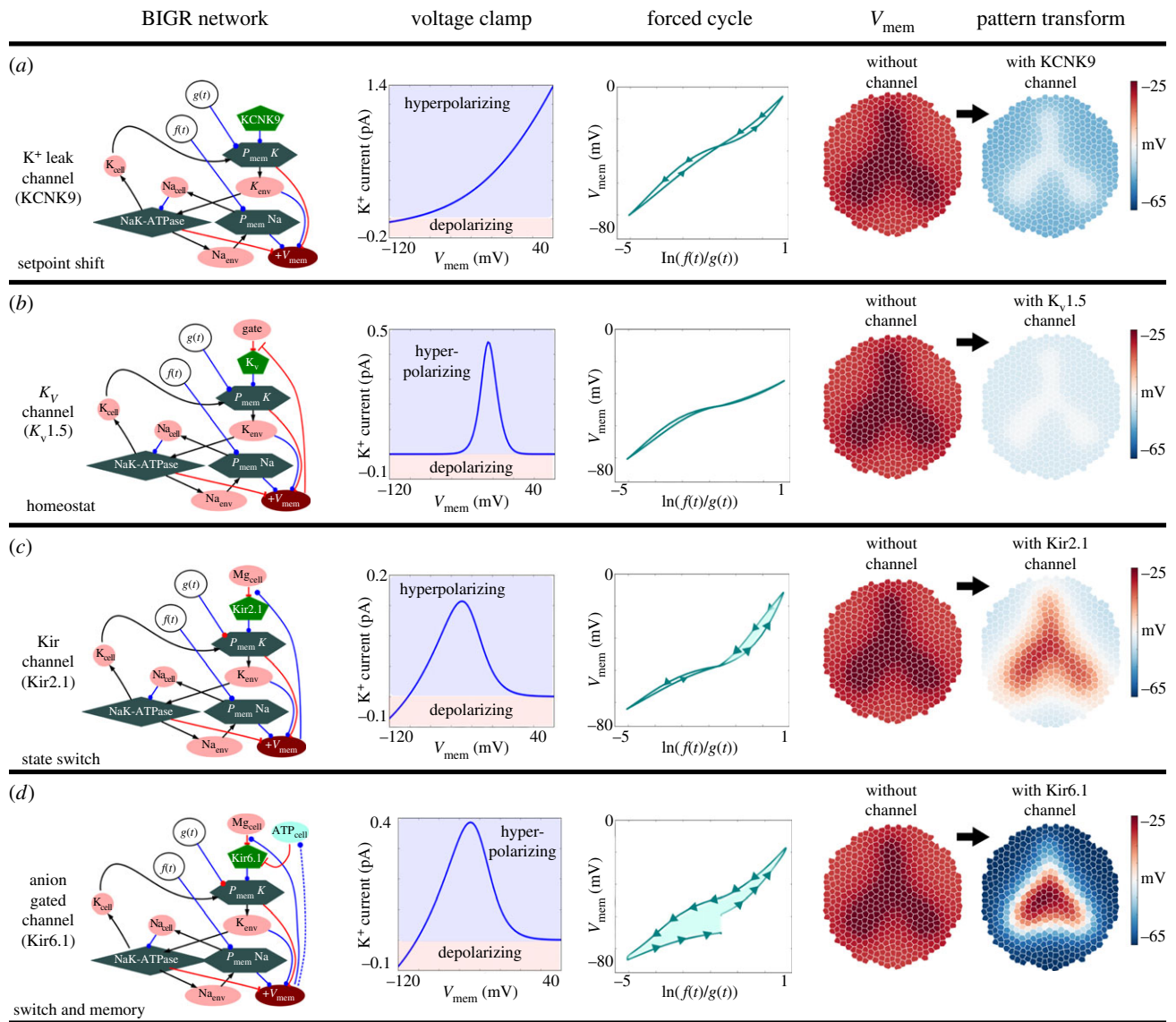


**Figure 3.**  $V_{mem}$ , ion channels and electrodiffusing gating ligand combinations create various functional network motifs exhibiting  $V_{mem}$  set-point shifting (a), homeostatic control of  $V_{mem}$  (b), selective state switching (c) and memory (d). (a) A straightforward  $K^+$  leak channel model (KCNK9), which has no additional regulation. (b) A simplified voltage-sensitive  $K^+$  channel model of a delayed-rectifier channel such as  $K_v$  1.5. The forced cycle curve of  $K_v$  shows virtually no hysteresis, and uniform  $K_v$  expression on cells of a cluster is predicted to flatten a  $V_{mem}$  pattern to a hyperpolarized setpoint, thereby demonstrating a homeostatic function of a  $K_v$  channel (b). (c) A  $K^+$  channel that is blocked by intracellular  $Mg^{2+}$  in a voltage-sensitive manner to generate a model of steady-state behaviour of the Kir 2.1 channel. The Kir 2.1 channel shows virtually no hysteresis, and uniform Kir 2.1 expression on cells of a cluster, and is predicted to increase the contrast of a slight  $V_{mem}$  pattern (c). (d) A  $K^+$  channel that is blocked by cytosolic  $Mg^{2+}$  in a  $V_{mem}$ -sensitive manner and is co-regulated by the anionic  $ATP^{4-}$  molecule to approximate a channel such as Kir6.1 or Kir6.2. The forced cycle curve of the ATP-Kir channel model shows hysteresis, indicating the channel has a memory, such that its present  $V_{mem}$  state is influenced by its previous  $V_{mem}$  experience (e). Uniform expression of ATP-Kir in cells of a cluster is predicted to dramatically increase the  $V_{mem}$  contrast and to alter the form of a slight preexisting  $V_{mem}$  pattern (e). Cell cluster simulations contained 487 GJ-coupled cells and measured 250  $\mu m$  in diameter.

double-headed (axial mirroring/duplication) phenotype by a transient block to GJ permeability. This planarian polarity control BGR network model is proposed as a simple, biologically plausible toy model to explore: (i) a role GJ coupling may serve in controlling anterior–posterior polarity control in planaria, by facilitating electrodiffusion of small charged molecules between cells in  $V_{mem}$  gradients, (ii) factors leading to emergent  $V_{mem}$  and correlated gene expression patterns, which can regenerate with appropriate polarity upon amputation, and (iii) the ability for  $V_{mem}$  to act as an instructive signal in a GRN in a biologically evidenced manner, in this case via control over polar transport. The BGR network model was run on GJ-coupled multicellular collectives of different sizes to ensure scalability, with the smallest model featuring 487 cells and measuring 400  $\mu m$  in length, and the largest model containing 1111 cells and measuring 1200  $\mu m$  in length. Full details (mathematical equations and parameter values) for the

planaria polarity control BGR network model can be found in the electronic supplementary material, S1.

## 2.5. Bioelectricity-integrated emergent $V_{mem}$ patterns network

A manual search of various BGR network configurations, with the aim of identifying realistic bioelectricity-integrated networks that could generate stable patterns of  $V_{mem}$  and correlated concentrations of signalling molecules, found that electrodiffusing charged molecules that directly gate ion channels in a self-reinforcing manner to be a system with clear capability to generate a range of stable patterns. A hypothetical BGR network capable of generating a wide range of patterns was selected on account of its simplicity (figure 5). The BGR network model was run on



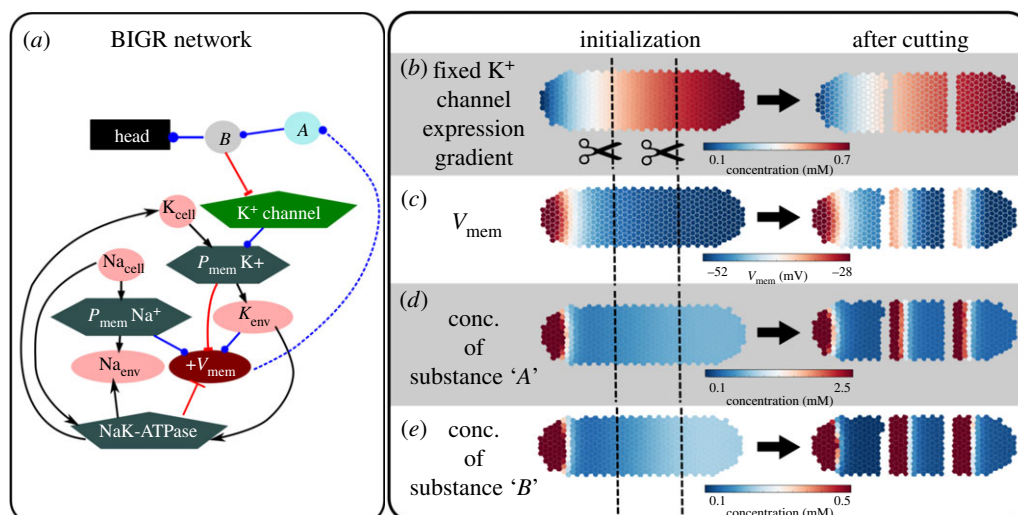


**Figure 4.** Electrodifusive transport of charged signalling molecules in GJ-coupled cell networks induces spontaneous formation of instructive  $V_{\text{mem}}$  gradients, which regenerate with cutting. The Bigr network for the model is shown in (a). Substance 'B' is proposed to be instructive for development of a head in a creature such as planaria (a). The initial state of the whole creature features a fixed anterior–posterior gradient of  $K^+$  channel expression, which generates a small fixed  $V_{\text{mem}}$  gradient along the axis of the worm, but being fixed is not altered by cutting or network dynamics (b). Positive feedback between electrodiffusion of anionic substance 'A' and the  $V_{\text{mem}}$  depolarizing effect of higher 'A' concentrations via growth of substance 'B', leads to the development of a stable  $V_{\text{mem}}$  gradient in the initialized state of the whole worm, and regeneration of gradients with the original polarity in each fragment of a worm cut into multiple pieces (c). The electrodiffusive transport of anion 'A' in the  $V_{\text{mem}}$  gradients of the GJ coupled cell network leads to enhanced concentration of substance 'A' at the anterior of the animal and in each fragment of the cut model (d), and growth of head-instructive substance 'B' in relation to higher concentration of 'A' (e). Cell cluster simulations contained 497 GJ-coupled cells and measured 400  $\mu\text{m}$  in length.

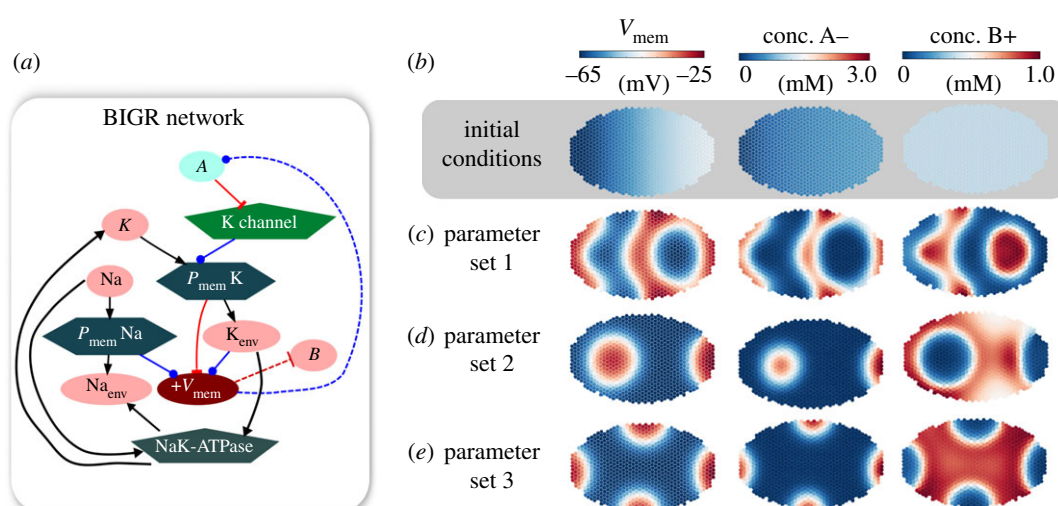


**Figure 5.** More complex steady patterns of  $V_{\text{mem}}$  and concentration are predicted to spontaneously evolve for electrodiffusing charged molecules that directly gate ion channels. The Bigr network shown in (a) involves electrodiffusion of an anionic substance 'A' from areas of hyperpolarized to depolarized  $V_{\text{mem}}$ , where substance 'A' also inhibits the activity of a  $K^+$  channel, generating a positive feedback between substance 'A' and  $V_{\text{mem}}$  (a). In the Bigr network, a cationic substance 'B' is included to illustrate the spontaneous pattern evolving for a GJ permeable cationic substance electrodiffusing in the cell network (a). The cell cluster features the initial conditions of a very slight concentration gradient of substance 'A', which generates a slight  $V_{\text{mem}}$  gradient associated with substance 'A' inhibition of the  $K^+$  channel, and a uniform concentration of substance 'B' (b). Different values of effective GJ diffusion constants ( $D_{\text{gj}}$ ) and Hill function describing the  $K^+$  channel gating properties ( $K_{1/2}$ ) were found to spontaneously evolve into different, stable patterns of stripes and spots (c,d). Parameter set 1 (c) used  $D_{\text{gj}}A = 1.0 \times 10^{-13} \text{ m}^2 \text{ s}^{-1}$  and  $K_{1/2} = 0.5 \text{ mM}$ , parameter set 2 (d) used  $D_{\text{gj}}A = 1.0 \times 10^{-12} \text{ m}^2 \text{ s}^{-1}$  and  $K_{1/2} = 0.5 \text{ mM}$ , and parameter set 3 (e) used  $D_{\text{gj}}A = 1.0 \times 10^{-12} \text{ m}^2 \text{ s}^{-1}$  and  $K_{1/2} = 0.7 \text{ mM}$ . The effective GJ diffusion constant of substance 'B' was fixed at  $D_{\text{gj}} = 1.0 \times 10^{-13} \text{ m}^2 \text{ s}^{-1}$ . Cell cluster simulations contained 882 GJ-coupled cells and measured 400  $\mu\text{m}$  in length.

GJ-coupled multicellular collectives with 882 cells, measuring a length of 400  $\mu\text{m}$ . The Bigr network shown in figure 5a models GJ-mediated intercellular electrodiffusion of an anionic substance 'A', where 'A' inhibits the activity of a  $K^+$  channel (figure 5a). Full details (mathematical equations and parameter values) for the stable bioelectric patterning Bigr network model can be found in the electronic supplementary material, S1.

## 3. Results

### 3.1. $V_{\text{mem}}$ integrates with regulatory networks by establishing steady-state concentrations

We first sought to establish a basic understanding of how spatial  $V_{\text{mem}}$  gradients interact with biochemical/genetic

**Table 1.** A summary of commonly occurring charged substances with known relationships to resting  $V_{\text{mem}}$  via their direct regulation of ion channels with ion leak characteristics. These substances may generate positive or negative feedback loops with respect to  $V_{\text{mem}}$ , and are therefore candidates for various functional network modalities including memory and homeostasis loops. 5HT3R, ionotropic serotonin receptor 3; 5HT2R, metabotropic serotonin receptor 2; nAChR, ionotropic nicotinic acetylcholine receptor; mAChR, metabotropic muscarinic acetylcholine receptor; NMDAR, *N*-methyl-D-aspartate receptor; KCNK, two-pore-domain  $\text{K}^+$  channel; ATP, adenosine triphosphate; NADP, nicotinamide adenine dinucleotide phosphate; WNT, Wingless-related integration site gene product family; Shh, Sonic hedgehog gene product; EGF, epidermal growth factor; aFGF, acidic fibroblast growth factor; bFGF, basic fibroblast growth factor.

substance	charge	channel	relationship	typical effect	reference
serotonin	+1	5HT3R	activating	depolarizing	[107]
		KCNK (via 5HT2R)	inhibiting	depolarizing	[93]
acetylcholine	+1	nicotinic (nAChR)	activating	depolarizing	[108]
		KCNK (via mAChR)	inhibiting	depolarizing	[93]
glutamate	−1	NMDA	activating	depolarizing	[109]
		chloride	activating	hyperpolarizing	[110]
calcium	+2	$\text{Ca}^{2+}$ gated $\text{K}^+$	activating	hyperpolarizing	[111]
		5HT3R	inhibiting	hyperpolarizing	[112]
magnesium	+2	NMDAR	inhibiting	depolarizing	[113]
		nicotinic (nAChR)	inhibiting	hyperpolarizing	[73]
		ATP-sensitive $\text{K}^+$	inhibiting	depolarization	[74]
zinc	+2	epithelial $\text{Na}^+$	activating	depolarizing	[114]
		NMDA	inhibiting	hyperpolarizing	[114]
ATP	−4	ATP-sensitive $\text{K}^+$	inhibiting	depolarization	[115]
NADP	−2	$\text{Ca}^{2+}$ gated $\text{K}^+$	inhibiting	depolarizing	[116]
WNT	+ <i>n</i> ( <i>pl</i> ≥ 9)	/	/	/	[117]
Shh	+ <i>n</i> ( <i>pl</i> ~ 8)	/	/	/	[118]
EGF	− <i>n</i> ( <i>pl</i> = 4.6)	/	/	/	[119]
aFGF	− <i>n</i> ( <i>pl</i> = 5.6)	/	/	/	[120]
bFGF	+ <i>n</i> ( <i>pl</i> = 9.6)	/	/	/	[120]

regulatory networks.  $V_{\text{mem}}$  has a significant influence on the concentration of charged ions inside and outside of cells, which may be a primary way  $V_{\text{mem}}$  integrates with, and exerts an influence on, regulatory networks. As summarized in table 1, in addition to common ions (e.g.  $\text{Na}^+$ ,  $\text{K}^+$ ,  $\text{Cl}^-$ ), a wide variety of charged substances exist in all biological systems including key small molecule regulators such as retinoic acid (negatively charged at physiological pH), many metabolites ( $\text{ATP}^{4-}$ ,  $\text{ATP-Mg}^{2-}$ ,  $\text{NADH}^{2-}$ ,  $\text{G6P}^{2-}$ ), neurotransmitters (serotonin<sup>+</sup>, glutamate<sup>−</sup>, acetylcholine<sup>+</sup>) and gene products (such as Hedgehog and Wnt proteins,  $\text{Hh}^{n+}$ ,  $\text{WNT}^{n+}$ ). Many of these charged substances regulate or co-regulate ion channels (table 1), and as ion channels control  $V_{\text{mem}}$  states, as will be discussed in the following, charged regulatory substances present numerous opportunities to participate in feedback loops between  $V_{\text{mem}}$  and substance concentration.

There are several mechanisms through which  $V_{\text{mem}}$  may influence the steady-state concentration profile of substances in the intra- and extracellular spaces (independent of genetic expression and chemical reactions). Firstly, all charged substances with finite membrane permeability are predicted to have steady-state concentration profiles that are significantly and directly established in relation to  $V_{\text{mem}}$  (figure 6a). This outcome can be derived by determining the steady-state solution of the GHK flux equation (equation (2.4)), which is a rearrangement of the well-known Nernst equation [78],

and is independent of the absolute value of the substance's transmembrane permeability:

$$\frac{c_i^{\text{cell}}}{c_i^{\text{env}}} = \exp\left(-\frac{z_i V_{\text{mem}} F}{RT}\right). \quad (3.1)$$

The rate at which the  $V_{\text{mem}}$ -dependent concentration equilibrium is reached is determined by the membrane permeability of the charged substance. Using equation (2.4) for a spherical cell with a radius of 5  $\mu\text{m}$ , a semi-membrane permeable molecule, such as an ionic reporter dye with membrane permeabilities of the order of  $1.0 \times 10^{-5} \text{ m s}^{-1}$  [121], with a charge of −2 and a fixed extracellular concentration of 1  $\mu\text{M}$ , is predicted to reach a steady-state cytosolic concentration of 24 nM for a  $V_{\text{mem}}$  of −50 mV in approximately 200 ms. However, even a highly impermeable molecule, such as an ion with the measured low base permeability of approximately  $1 \times 10^{-10} \text{ m s}^{-1}$  [122], is predicted to reach the same steady-state concentration of 24 nM in a longer time of 6 h—a time scale that remains relevant to the dynamic processes of development and regeneration. Most small charged molecules (including cell metabolites and pharmacological agents) can be expected to have membrane permeabilities falling between these two extremes.

Secondly, as  $V_{\text{mem}}$  controls the open/closed state of voltage-sensitive  $\text{Ca}_v$  channels,  $V_{\text{mem}}$  can act as a key regulator of ubiquitous secondary-messenger  $\text{Ca}^{2+}$  in cells expressing  $\text{Ca}_v$

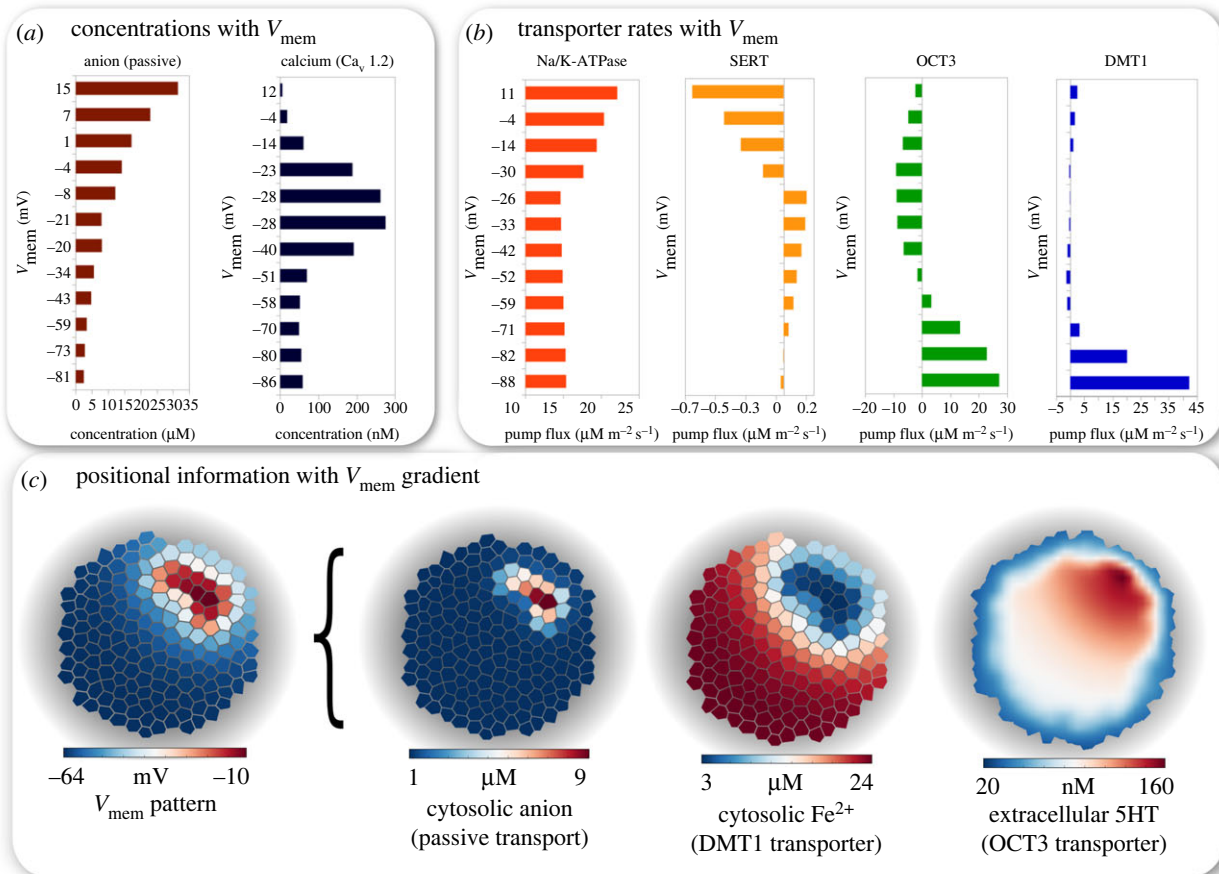


**Figure 6.**  $V_{\text{mem}}$  is predicted to influence rates of passive and active transport of charged substances, to establish  $V_{\text{mem}}$ -dependent steady-state concentrations of substances inside and outside of cells. Predicted effect of  $V_{\text{mem}}$  on the steady-state concentration of charged substances passively diffusing across the membrane (a). As  $V_{\text{mem}}$  also controls the open/closed state of voltage-gated  $\text{Ca}^{2+}$  channels, cytosolic  $\text{Ca}^{2+}$  levels are predicted to show high correspondence to resting  $V_{\text{mem}}$  for cells expressing channels such as the L-type  $\text{Ca}_v1.2$  (a).  $V_{\text{mem}}$  is also predicted to directly influence the rate of certain ion pumps and transmembrane transporters (b). The ability for resting  $V_{\text{mem}}$  to influence rates of passive and active transport enables patterns of  $V_{\text{mem}}$  to generate downstream positional information (c). In (c), a  $V_{\text{mem}}$  pattern was created by forcing cells in the top right to have a higher ratio of  $P_{\text{mem}}^{\text{Na}}:P_{\text{mem}}^{\text{K}} = 5:1$  than cells in the remaining cluster where  $P_{\text{mem}}^{\text{Na}}:P_{\text{mem}}^{\text{K}} = 1:25$ . The pattern of  $V_{\text{mem}}$  is predicted to be capable of establishing correlated patterns of key substances in relation to  $V_{\text{mem}}$  depolarization (c).

channels (figure 6a). Furthermore, charged substances transported across membranes by active (i.e. ATP consuming) ion pumps such as the  $\text{Na}^+/\text{K}^+$ -ATPase have rates that are predicted to be dependent on resting  $V_{\text{mem}}$ , as shown in figure 6b. In addition, facilitated transporters such as the SERT (predicted rates with various resting  $V_{\text{mem}}$  shown in figure 6b), the organic cation transporters (OCT3) moving both positively charged serotonin (5HT) or acetylcholine out of the cell (figure 6b), and the divalent metal transporter (DMT1) moving positively charged  $\text{Fe}^{2+}$  and  $\text{Zn}^{2+}$  into cells (figure 6b) are predicted to have rates, and therefore values of steady-state substance concentrations, to be significantly influenced by resting  $V_{\text{mem}}$  (figure 6b). Note that consistent with the above modelled ion pump/transporter results, similar  $V_{\text{mem}}$ -sensitivity has been experimentally reported for the OCT3 transporter [87], the  $\text{Na}^+/\text{K}^+$ -ATPase pump [83,123], the DMT1 transporter [90] and the SERT transporter under conditions of low extracellular  $\text{Cl}^-$  and absence of  $\text{Cl}^-$  related transporters (consistent conditions for the above model) [84,124].

These direct relationships between steady-state concentration levels of charged ions/molecules in cells and resting  $V_{\text{mem}}$  demonstrate how  $V_{\text{mem}}$  can rapidly (on the scale of seconds to minutes) and directly establish cytosolic and extracellular levels of those charged species and thereby lead to profiles of positional information that are functionally

integrated with spatial  $V_{\text{mem}}$  patterns (figure 6c). Therefore, transmembrane voltage distributions, which can be controlled by numerous available modalities (pharmacological, genetic, optogenetic, etc.), can be used to manipulate gradients of key biochemical signalling molecules, establishing specific foci or distribution patterns as needed for experimental or therapeutic applications.

### 3.2. $V_{\text{mem}}$ controls memory, homeostat and switch network moieties

One of the key properties of many living things is the ability to maintain a pattern memory that enables remodelling to proceed towards a specific (correct) target morphology [3]. This is observed during regeneration of appendages and other organs in models like salamander [125], as well as during the regulation of embryogenesis to a normal body despite 'cut-and-paste' experiments during early stages of development [126,127]. Given that bioelectric states are an important driver of patterning, we next sought to explore their robustness properties, their stability to perturbation and their ability to maintain a history of prior state. Owing to the ubiquitous occurrence of various classes of  $\text{K}^+$  channels in somatic cell systems and their significant role in developmental processes such as size regulation [128], oncogenic dysmorphias [129] and multi-organ patterning



[130–132], we chose to construct and analyse bioelectric network moieties based on different  $K^+$  channel arrangements, specifically including a number of channels that have been shown to play important roles in pattern control via functional studies or human channelopathies.

As shown in figure 3, our analysis determined that simple networks involving feedback relationships between  $V_{\text{mem}}$ ,  $K^+$  channel state and electrodiffusing gating ligand combinations can create various functional network motifs exhibiting different kinds of behaviour including:  $V_{\text{mem}}$  set-point shifting (figure 3a), homeostatic control of  $V_{\text{mem}}$  (figure 3b), selective state switching of  $V_{\text{mem}}$  (figure 3c) and memory of  $V_{\text{mem}}$  state (figure 3d).

Figure 3a shows a straightforward  $K^+$  leak channel model (based on the channel KCNK9 [93]), which is not subject to any additional regulation. Analysis showed that the KCNK9 model exhibits a monotonically increasing and primarily hyperpolarizing voltage clamp curve, virtually no hysteresis and uniform KCNK9 expression on a cell cluster is predicted to uniformly alter  $V_{\text{mem}}$  of cells to transition a pattern to a hyperpolarized set-point (figure 3a). Therefore, the functionality enabled by a leak channel such as the KCNK9 is a simple shift of the resting  $V_{\text{mem}}$  set-point of a cells to a new value (figure 3a).

A homeostat describes a device that maintains a parameter at a singular value and is capable of resisting change from perturbations. Figure 3b shows a simplified voltage-sensitive  $K^+$  channel model, with characteristics based on the steady-state behaviour of a delayed-rectifier channel such as  $K_V1.5$  [76]. The  $K_V1.5$  has a positively charged extracellular protein gate, which due to voltage-sensitive interactions at the membrane, becomes more effective at closing the channel at hyperpolarized  $V_{\text{mem}}$ . The  $K_V1.5$  model's voltage clamp curve shows no conductivity (closed channel) below a  $V_{\text{mem}}$  of approximately  $-40$  mV, followed by channel opening and increasing hyperpolarization of  $V_{\text{mem}}$  with increasing states of  $V_{\text{mem}}$  depolarization (figure 3b). The forced cycle curve of  $K_V1.5$  shows virtually no hysteresis. Uniform  $K_V1.5$  expression on cells of a cluster is predicted to flatten a  $V_{\text{mem}}$  pattern to a hyperpolarized value of approximately  $-40$  mV (figure 3b), thereby demonstrating a homeostatic function of the  $K_V1.5$  channel (B). The homeostatic effect of the  $K_V1.5$  channel occurs as the channel has an increased degree of opening at more depolarized  $V_{\text{mem}}$ , with the effect of hyperpolarizing  $V_{\text{mem}}$  with channel opening. Experimentally, the  $K_V1.5$  channel has been used to induce defects in brain patterning and eye induction by flattening a physiologically essential  $V_{\text{mem}}$  gradient to a uniform hyperpolarization [41,48], which is consistent with the homeostat functionality implied by our bioelectric network simulations.

Figure 3c shows a  $K^+$  channel that is blocked by intracellular  $Mg^{2+}$  in a voltage-sensitive manner [74] to generate a model of steady-state behaviour of the Kir2.1 channel. The voltage-sensitivity of the  $Mg^{2+}$  block means  $Mg^{2+}$  is more effective at blocking the channel at depolarized voltages [74]. The Kir2.1 model voltage clamp curve shows the expected form for the Kir2.1 channel [133] with depolarization at  $V_{\text{mem}}$  below  $-100$  mV, hyperpolarizing between  $-100$  mV and  $-20$  mV, and no effect on  $V_{\text{mem}}$  for  $V_{\text{mem}}$  above  $-10$  mV (figure 3c). The Kir2.1 channel shows virtually no hysteresis, while uniform Kir2.1 expression on cells of a cluster is predicted to increase the contrast of a slight  $V_{\text{mem}}$  pattern by preferentially hyperpolarizing cells that are more hyperpolarized, while leaving more

depolarized cells untouched (figure 3c). Such contrast-enhancing functions are an important property for enforcing boundaries between adjacent compartments with distinct  $V_{\text{mem}}$ , explaining their central role in establishing bioelectrical pre-patterns of diverse organ primordia such as those in the nascent face [40].

The form of the voltage clamp curve for the K-ATP channel model (based on ATP co-regulated channels Kir6.1 and Kir6.2 [134]) was similar to that of the Kir2.1 model (figure 3d). The forced cycle curve of the K-ATP channel model shows hysteresis, indicating the channel has a memory, such that its present  $V_{\text{mem}}$  state is influenced by its previous  $V_{\text{mem}}$  experience ( $E$ ). The hysteresis and memory of the K-ATP channel model occurs because anionic  $ATP^{4-}$  can, via electrodiffusion, move in the absence of a concentration gradient through GJ from more hyperpolarized to depolarized regions, and  $ATP^{4-}$  inhibits the hyperpolarizing channel to promote  $V_{\text{mem}}$  depolarization. The uniform expression of K-ATP to a cell cluster is predicted to dramatically increase the  $V_{\text{mem}}$  contrast and to alter the form of a slight preexisting  $V_{\text{mem}}$  pattern ( $E$ ). Experimentally, K-ATP has been implicated in the establishment of sharp  $V_{\text{mem}}$  boundaries and in the foundation of key bioelectrical pre-patterns, such as those in the developing brain and eye [41,48] and left–right symmetry [135].

Interestingly, positive feedback between  $V_{\text{mem}}$  and a charged substance concentration, which may happen in a variety of circumstances including a negatively charged, GJ-permeable substance in the cytosol blocking a hyperpolarizing  $K^+$  ion channel (figure 3d), establishes a bioelectric memory. As a function of the  $P_{\text{mem}}^{\text{Na}} : P_{\text{mem}}^{\text{K}}$  control parameter, the forced cycle curve exposes a bioelectric memory for this network configuration, as the forwards and reverse paths are not equivalent, but form a classical hysteresis loop (figure 3d). The area of the loop is indicative of the degree of memory in the system. Note that the hysteresis implicit in the flexible  $V_{\text{mem}}$  memory dynamics is independent of initial state: if the initial  $V_{\text{mem}}$  of the cell is depolarized, sufficiently strong hyperpolarization will result in a memory of the hyperpolarization, where subsequent strong depolarizations will erase the memory and return  $V_{\text{mem}}$  to its original value. These results help to understand an otherwise extremely puzzling phenomenon: the ability of tissues to represent specific target morphologies for regenerative outcomes that can be edited or re-written, as has been observed in deer antlers, crab claws and planarian head–tail patterning (reviewed in [136]). They also reveal a simple network that can be exploited in synthetic biology applications for implementing state in bioengineered constructs.

While set-point shifting, homeostatic state control, state-switching and memory functions are shown here with respect to various specific  $K^+$  channel examples, it is notable that there are several alternative bioelectric configurations that can exhibit these same functions. As  $V_{\text{mem}}$  is indicated to influence the steady-state concentration of ionic substances inside and outside of cells (figure 6), the fact that charged substances can also act as gating ligands (table 1) establishes conditions for simple feedbacks to be created between  $V_{\text{mem}}$  and the intra- or extracellular concentrations of charged substances. These feedback relationships give each network motif a characteristic functionality and can be thought of as meta-structure elements similar to the electronic components on a circuit board. Feedback loops are known to be a key component of amplification and stabilization in complex systems, and are likely to underlie memory and homeostatic properties. These

intrinsic dynamics for bioelectric circuits enable evolution to select from a wide range of electrogenic gene products (e.g. protein-based ion pumps and channels) and ligands, implementing functionality as needed for the robust patterning observed during development and regeneration.

### 3.3. Gap junctions enable scale-free spontaneous regeneration of instructive $V_{\text{mem}}$ gradients

We next sought to illustrate the power of BIGR networks by producing a quantitative, constructive model of planarian-like regeneration, a model system whose remarkably robust regenerative behaviour has challenged scientists for over 120 years [102,104,137]. One of the key properties of planarian flatworms is that when cut, each piece produces exactly what is missing at each wound edge. It rescales and maintains its normal anterior–posterior polarity. Some diffusion-based models have been produced [62,63,138], and recent data showed the importance of bioelectrics for this process by producing double-headed or no-headed (i.e. double-tailed) worms [38,42,139] by manipulating the  $V_{\text{mem}}$  gradients and the GJ connectivity within the fragment. Nevertheless, the ability for the two wounds on either side of a single bisection to make radically different structures—a head and a tail—is still largely a mystery, as the two regions of the wound shared the same positional information values prior to the bisection. To move beyond the current state of the art requires a model that both explains the large scale (logic) of the algorithm that provides this kind of robust re-patterning. For this reason, we constructed a generalized spatialized model that manifests the required capabilities while requiring only a low-level axial gradient of a single network substance concentration. A much more complete version of a planaria-specific model will be presented in a forthcoming paper. Here our goal is to illustrate the principles of bioelectrics and the new modelling environment via a minimal model that shows the dynamics sufficient to implement the observed regenerative properties.

We have described  $V_{\text{mem}}$  as an instructive signal with the ability to alter regulatory network state by influencing the steady-state concentrations of charged substances via transmembrane passage rates (figures 6 and 2). However, for multicellular networks where cells are coupled via GJs, the influence of  $V_{\text{mem}}$  extends beyond the plasma membrane to a spatial dimension, such that charged substances can be drawn through the cell network by  $V_{\text{mem}}$  gradients between cells (figure 4b). We demonstrate the effect of these abilities for  $V_{\text{mem}}$  to influence concentrations, and thereby dramatically change regulatory network state, using the BIGR network designed to describe simple aspects of bioelectrical signalling in planaria (figure 4a) running on an elliptical cell collective. In this model, a patch of depolarized  $V_{\text{mem}}$  at the far right of the elliptical cell cluster establishes conditions to create distinct patterns of gene expression, which are directly correlated to the  $V_{\text{mem}}$  pattern in the collective (figure 4).

The BIGR network designed to describe integrated bioelectrical signalling and gene expression in planaria regeneration (figure 4a) is not simply instructive of downstream genetic outcomes, but shows advanced dynamics allowing the cell collective to spontaneously form and reform the instructive depolarized  $V_{\text{mem}}$  region at one end. In a full model, the network spontaneously forms a depolarized  $V_{\text{mem}}$  region at the far right of the elliptical cluster (figure 4c) that coincides with

key regulatory substances instructive for the formation of a head (figure 4d,e). The system works on the basis of a built-in ion channel expression gradient along the anterior–posterior axis of the elliptical model (figure 4b) leading to the formation of a low-level  $V_{\text{mem}}$  gradient along the long axis of the model. This low-level fixed  $V_{\text{mem}}$  gradient leads to electrodiffusive passage of anionic substance 'A' along the long axis—an experimentally confirmed phenomenon that is critically dependent on functional GJ [140–143]. In turn, the anion 'A' activates production of substance 'B', which inhibits a  $K^+$  ion channel (figure 4a). Therefore, as 'A' moves through the cell collective, it significantly amplifies the  $V_{\text{mem}}$  gradient along the long axis, leading to positive feedback with more 'A' being electrophoretically drawn to the anterior pole, ultimately forming a region of strong depolarization and high 'A' and 'B' concentrations at the far left (figure 4c–e). When the model is cut anywhere along its long axis, the dynamics of the system work in the same manner described above to recreate depolarized  $V_{\text{mem}}$  regions with the original polarity in each remaining fragment (figure 4c–e). In addition, the dynamics of cell clusters running the BIGR network in figure 4a are independent of model scale, with models demonstrating the ability to capture the exact same behaviour for the same BIGR network and the same model parameters for a very wide range of sizes (figure 7a). Moreover, blocking GJs after cutting is predicted to produce the expected double-headed phenotype, as blocked GJs inhibit the electrodiffusive transport of anionic substance 'A', leading to growth of substance 'A' to its equilibrium level and uniform growth of substance 'B' across each fragment (figure 7b). The electronic supplementary material, S1, outlines further details of this model.

### 3.4. Ion channels gated by electrodiffusing ligands identified as fundamental mechanism for stable $V_{\text{mem}}$ pattern generation

In searching for realistic bioelectrical networks with the capacity to generate stable patterns of  $V_{\text{mem}}$  and correlated concentrations of signalling molecules, we identified electrodiffusing charged molecules that directly gate ion channels as a system with clear patterning capacity (figure 5). The BIGR network shown in figure 5a predicts that GJ-mediated intercellular electrodiffusion of an anionic substance 'A' will spontaneously occur from areas of hyperpolarized to depolarized  $V_{\text{mem}}$ . However, substance 'A' also inhibits the activity of a  $K^+$  channel, generating depolarized  $V_{\text{mem}}$  in regions where substance 'A' accumulates, thereby establishing a positive feedback between substance 'A' and  $V_{\text{mem}}$  (figure 5a). In the BIGR network shown in figure 5a, a cationic substance 'B' is included to illustrate the spontaneous concentration pattern evolving for a GJ permeable cationic substance electrodiffusing in the cell network, although 'B' does not participate in any regulation or reaction dynamics (figure 5a). The cell cluster features the initial condition of a very slight concentration gradient of substance 'A', which generates a slight  $V_{\text{mem}}$  gradient associated with substance 'A' inhibition of the  $K^+$  channel, and a uniform concentration of substance 'B' (figure 5b). No production gradients or fixed heterogeneities were employed. Different values of effective GJ diffusion constants ( $D_{\text{gi}}$ ) and Hill function describing the  $K^+$  channel gating properties ( $K_{1/2}$ ) were found to spontaneously evolve into different, stable patterns of resting  $V_{\text{mem}}$  stripes and spots (figure 5c,d), for the

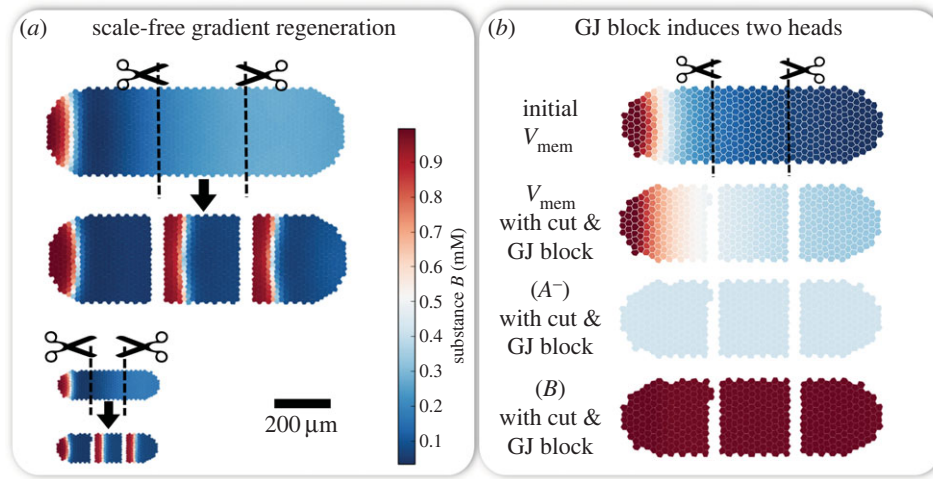


**Figure 7.** The spontaneous regeneration of instructive  $V_{\text{mem}}$  gradients occurs independent of model size, but is dependent on functional GJs. The BIGN network designed to describe integrated bioelectrical signalling and gene expression in planaria regeneration can spontaneously reform  $V_{\text{mem}}$ , and 'A' and 'B' concentration gradients in each fragment of a cut model for all model sizes examined, and is therefore predicted to be a scale-free model (a). Blocking GJ after cutting inhibits the electrodiffusive transport of anionic substance 'A', leading to growth of substance 'A' to its equilibrium level and uniform growth of substance 'B' across each fragment, which predicts the expected anatomical outcome of two heads with GJ blocking (b).

exact same BIGN network and initial conditions shown in figure 5a,b. Parameter set 1 (figure 5c) used  $D_{\text{gj}}A = 1.0 \times 10^{-13} \text{ m}^2 \text{ s}^{-1}$  and  $K_{1/2} = 0.5 \text{ mM}$ , parameter set 2 (figure 5d) used  $D_{\text{gj}}A = 1.0 \times 10^{-12} \text{ m}^2 \text{ s}^{-1}$  and  $K_{1/2} = 0.5 \text{ mM}$ , and parameter set 3 (figure 5e) used  $D_{\text{gj}}A = 1.0 \times 10^{-12} \text{ m}^2 \text{ s}^{-1}$  and  $K_{1/2} = 0.7 \text{ mM}$ . The effective GJ diffusion constant of substance 'B' was fixed at  $D_{\text{gj}} = 1.0 \times 10^{-13} \text{ m}^2 \text{ s}^{-1}$  for all scenarios. The electronic supplementary material, S1, outlines further details of this model. Note that there are numerous possibilities for patterning networks involving different kinds of ion channels (and even electrogenic pumps or transporters) that are regulated by charged substances which introduce similar feedbacks to the model explored in figure 5. Thus, from these results, we conclude that BIGN networks can lead to the spontaneous emergence of complex physiological patterns within tissues—an important capability for understanding the ubiquitous increase of order during embryogenesis and regeneration where instructive  $V_{\text{mem}}$  patterns have been experimentally observed [39,41,48].

## 4. Discussion

Bioelectric signals such as  $V_{\text{mem}}$  play well-demonstrated roles in development, regeneration and disease; yet, the dynamics and capabilities of bioelectric signals in tissues are poorly understood, and a key knowledge gap exists between the well-understood voltage properties of single cells and the control of large-scale anatomical patterns by  $V_{\text{mem}}$ . In order to better understand the roles of  $V_{\text{mem}}$  in the emergence and regulation of biochemical positional information patterns, we have considered two fundamentally different network-based dynamic systems: (i) the mixed regulatory signals and agents of BIGN network models, which arise in single cells and (ii) spatial networks comprised of GJ coupled biological cells supporting BIGN networks, where cells are the nodes of the network. Both of these different network types are crucially important to the formation and regulation of biological pattern.

In our planaria polarity control model (figure 4), we have shown how genetically identical cells with the same initial

proteomic profiles can proceed to fundamentally different outcomes when cells simply receive different  $V_{\text{mem}}$  signals, where the specific nature of the outcomes depends on the characteristics of the BIGN network. One of the major open questions in developmental and regenerative biology is where pattern comes from. It is well known that anatomy is not directly encoded by the genome, but fundamental gaps exist in our knowledge of how pattern emerges via the interplay between physics and genetics, what patterns could arise from a standard cellular genome (under different epigenetic conditions), and what might be convenient control points at which such systems could be efficiently manipulated to produce desired patterning outcomes (guided self-assembly). We demonstrate that stable patterns of positional information (and subsequent patterning outcomes) can be edited solely by altering bioelectric signals without changing gene expression directly. Our BIGN network models illustrate precisely how the physiological layer of pattern control has its own intrinsic dynamics that are not reducible to mRNA or protein profiles.

Our *in silico* simulations indicate that the influence of  $V_{\text{mem}}$  in regulatory networks can occur independently of transcriptional or translational changes. The interesting recent work of Cervera *et al.* [66] proposes a feedback relationship to exist as a (non-specified) relationship between  $V_{\text{mem}}$  and genetic expression of ion channels, which leads to changes in ion channel expression and membrane permeability with associated changes in  $V_{\text{mem}}$ . Our models predict straightforward, direct and specific means through which  $V_{\text{mem}}$  can alter gene or reaction regulatory network state, such as the capability for  $V_{\text{mem}}$  to alter transmembrane passage rates of charged substances (figure 6), thereby influencing the steady-state concentration profiles of regulatory molecules to shift entire network states into concentration and gene expression patterns which are functionally integrated with the  $V_{\text{mem}}$  patterns arising in the cell network (figures 4 and 5). Additionally, we predict that BIGN network models can generate direct feedbacks between  $V_{\text{mem}}$  and substances of the network, which develop specific functionalities such as the ability to write flexible  $V_{\text{mem}}$  memory, and homeostatic control of  $V_{\text{mem}}$  state against perturbation (figure 3). Feedback between  $V_{\text{mem}}$  state and key molecular-genetic regulators has been



observed with Pax6 in eye development [48] and Notch in brain patterning [41].

We further indicate how electrodiffusive passage of substances through the GJ coupled cell network enables the spontaneous emergence of instructive  $V_{\text{mem}}$  gradients, which regenerate with the original polarity in each fragment of a cut model (figure 4). These emergent models work as GJ create intercellular coupling between cells, so that the influence of  $V_{\text{mem}}$  can extend beyond individual plasma membranes to affect the cell collective as a whole, spontaneously *creating* concentration gradients and more complex patterns from homogeneous initial states (figures 4 and 5). Furthermore,  $V_{\text{mem}}$  gradients may supply a directional transport impetus that is virtually independent of scale (figure 7), making electrodiffusive transport of charged morphogenic substances a phenomenon that enables, or at least simplifies, mechanisms involved in the regeneration of key anatomical axes upon serious perturbation. Notably, a model proposing the electrophoresis of a large (200–400 kDa), electronegative protein ( $pI \sim 5$  at pH 7.0) produced in the head and inhibiting head regeneration was proposed nearly 40 years ago by Lange *et al.* [64] to explain polarity control in planaria; however, the identity of this large, negative protein has never been determined.

Given their importance in the control of gene expression and anatomical change, how can the dynamics of bioelectrical networks be rationally modulated? As values of  $V_{\text{mem}}$  are predicted to be a key instructive factor in the behaviour of BIGR networks, the ability to practically manipulate  $V_{\text{mem}}$  is very important. While there are several ways to control resting  $V_{\text{mem}}$ , including by altering activities of expressed ion pumps and transporters, and by manipulating any expressed chloride channels, the  $P_{\text{mem}}^{\text{Na}} : P_{\text{mem}}^{\text{K}}$  is a clear target for resting  $V_{\text{mem}}$  manipulations, which applies to most cell types. The  $P_{\text{mem}}^{\text{Na}} : P_{\text{mem}}^{\text{K}}$  is a general predictor of resting  $V_{\text{mem}}$  as most eukaryotic cells have an enzymatic  $\text{Na}^+/\text{K}^+$ -ATPase ion pump [78]. Our analyses predict that manipulation of  $P_{\text{mem}}^{\text{Na}} : P_{\text{mem}}^{\text{K}}$  is a powerful therapeutic strategy (indeed, the importance of the sodium:potassium ratio has long been known as an important factor in cancer induction [144,145]). Voltage-gated channels with considerable conductivity at typical cell resting potentials, including inward-rectifying  $\text{K}^+$  channels (Kir) and channels from the HCN family, may also serve as effective targets for somatic bioelectrical manipulations [146,147]. Notably, the above listing focuses on channels capable of modifying the  $P_{\text{mem}}^{\text{Na}} : P_{\text{mem}}^{\text{K}}$  ratio; however,  $V_{\text{mem}}$  manipulations can be achieved through a wide range of additional means, including pharmaceutically induced modifications to chloride channels and alterations of ion pump and other transporter rates. Furthermore, an ever-increasing toolkit of optogenetic [32], magnetogenetic [148] and microfluidic [149] reagents are becoming available for modulating bioelectric state *in vivo* and *in vitro*.

Modelling bioelectricity in somatic cell networks is an emerging field of study that is also being considered by other researchers, who have revealed important characteristics of GJ-coupled cell networks and the role of biochemical interventions [66,150,151]. A primary difference of our BETSE modelling platform is that instead of an equivalent circuit model of bioelectricity, we determine bioelectrical states and signals in terms of the more fundamental substance concentrations inside and outside of cells [65]. By describing bioelectricity in terms of fundamental substance concentrations

and fluxes, the full capabilities of reaction (electro)diffusion and GRN are embedded into our models. This intimately links bioelectrical and biochemical states, provides a clear connection to experimentally accessible variables, and allows for a realistic depiction of ion pumps, channels and a variety of transmembrane transporters such as SERT and DMT1. Thus, the BETSE platform complements existing equivalent circuit models of bioelectricity which simplify the bioelectrical system using adaptations to electrical circuit formula [66], and therefore do not directly consider electrodiffusive transport of ions and other substances through multiple routes of a heterogeneous cell network, nor allow for the inclusion of complex regulatory networks (which are all capabilities of our existing BETSE platform). There are, however, several limitations with our current approach, which will be improved with future developments of our modelling platform. For example, cell proliferation is a major component of pattern formation in developing and regenerating biological systems; subsequent versions of the BETSE environment will enable simulation of proliferative growth and apoptosis, and will allow users to explore the role of mechanical movements of cells and tissues in the development of pattern.

In future work, additional enhancements are planned to facilitate automated discovery of networks with desired patterning behaviour (to assist in synthetic bioengineering applications), to quantify evolvability of networks with specific patterning properties, and quantify and visualize high-level control metrics like integrated information [152]. Most importantly, we are currently building detailed models of specific patterning contexts, including planarian regeneration, cancer progression and craniofacial patterning during development. The quantitative analysis of their BETSE networks will enable better prediction and control of real biological systems, and may facilitate novel interventions in regenerative medicine [40,51]. Moreover, analysis of these first fully specified, generative models will help reveal new aspects of self-organization and global dynamics that characterize the remarkably powerful interplay of genetic and biophysical signalling.

**Data accessibility.** Fully open code and documentation for the BETSE software program are available from the online repository: <https://gitlab.com/betse/betse>. The BETSE software will run the model files supplied in the electronic supplementary material and exploration of user-defined BIGR network models.

**Authors' contributions.** M.L. contributed to project conceptualization, funding acquisition and strategic guidance on specific directions for investigation. A.P. contributed methodology (design and development of models), investigation, software development and formal analysis. A.P. and M.L. wrote the manuscript together.

**Competing interests.** The authors declare no conflicts of interest.

**Funding.** This work was supported by an Allen Discovery Center award from the Paul G. Allen Frontiers Group (12171). The authors gratefully acknowledge support from the National Institutes of Health (AR055993, AR061988, HD81401), the G. Harold and Leila Y. Mathers Charitable Foundation (TFU141), National Science Foundation award no. CBET-0939511, the W. M. KECK Foundation (5903) and the Templeton World Charity Foundation (TWCFO089/AB55).

**Acknowledgments.** The authors express gratitude to Dany S. Adams of Tufts University, Joshua Finkelstein of the Allen Discovery Center at Tufts University, Patrick McMillen of Tufts University, Pai Vaibhav of Tufts University and Jessica Whited of Harvard Medical School, for their very helpful advice and commentary during the construction of this paper. Sincere thanks to Cecil Curry for his extensive assistance with BETSE software development.

## References

- Baddour JA, Sousounis K, Tsonis PA. 2012 Organ repair and regeneration: an overview. *Birth Defects Res. C Embryo Today* **96**, 1–29. (doi:10.1002/bdrc.21006)
- Birnbaum KD, Sánchez Alvarado A. 2008 Slicing across kingdoms: regeneration in plants and animals. *Cell* **132**, 697–710. (doi:10.1016/j.cell.2008.01.040)
- Levin M. 2012 Morphogenetic fields in embryogenesis, regeneration, and cancer: non-local control of complex patterning. *Biosystems* **109**, 243–261. (doi:10.1016/j.biosystems.2012.04.005)
- Turing AM. 1952 The chemical basis of morphogenesis. *Phil. Trans. R. Soc. Lond. B* **237**, 37–72. (doi:10.1098/rstb.1952.0012)
- Wolpert L. 1969 Positional information and the spatial pattern of cellular differentiation. *J. Theor. Biol.* **25**, 1–47. (doi:10.1016/S0022-5193(69)80016-0)
- Blackstone NW. 2008 Metabolic gradients: a new system for old questions. *Curr. Biol.* **18**, R351–R353. (doi:10.1016/j.cub.2008.03.039)
- Green JBA, Sharpe J. 2015 Positional information and reaction–diffusion: two big ideas in developmental biology combine. *Development* **142**, 1203–1211. (doi:10.1242/dev.114991)
- Meinhardt H. 2008 Models of biological pattern formation: from elementary steps to the organization of embryonic axes. *Curr. Top. Dev. Biol.* **81**, 1–63. (doi:10.1016/S0070-2153(07)81001-5)
- Slack J. 2014 Establishment of spatial pattern. *Wiley Interdiscip. Rev. Dev. Biol.* **3**, 379–388. (doi:10.1002/wdev.144)
- Karlebach G, Shamir R. 2008 Modelling and analysis of gene regulatory networks. *Nat. Rev. Mol. Cell Biol.* **9**, 770–780. (doi:10.1038/nrm2503)
- Annunziata R, Arnone MI. 2014 A dynamic regulatory network explains ParaHox gene control of gut patterning in the sea urchin. *Development* **141**, 2462–2472. (doi:10.1242/dev.105775)
- Beccari L, Marco-Ferreres R, Bovolenta P. 2013 The logic of gene regulatory networks in early vertebrate forebrain patterning. *Mech. Dev.* **130**, 95–111. (doi:10.1016/j.mod.2012.10.004)
- Cavalieri V, Spinelli G. 2014 Early asymmetric cues triggering the dorsal/ventral gene regulatory network of the sea urchin embryo. *eLife* **3**, e04664. (doi:10.7554/eLife.04664)
- Uzkudun M, Marcon L, Sharpe J. 2015 Data-driven modelling of a gene regulatory network for cell fate decisions in the growing limb bud. *Mol. Syst. Biol.* **11**, 815. (doi:10.15252/msb.20145882)
- Jhamb D, Rao N, Milner DJ, Song F, Cameron JA, Stocum DL, Palakal MJ. 2011 Network based transcription factor analysis of regenerating axolotl limbs. *BMC Bioinformatics* **12**, 80. (doi:10.1186/1471-2105-12-80)
- Schiffmann Y. 2004 Segmentation and zooid formation in animals with a posterior growing region: the case for metabolic gradients and Turing waves. *Prog. Biophys. Mol. Biol.* **84**, 61–84. (doi:10.1016/S0079-6107(03)00059-2)
- König M, Holzhütter HG, Berndt N. 2013 Metabolic gradients as key regulators in zonation of tumor energy metabolism: a tissue-scale model-based study. *Biotechnol. J* **8**, 1058–1069. (doi:10.1002/biot.201200393)
- Watson E, MacNeil LT, Arda HE, Zhu LJ, Walhout AJM. 2013 Integration of metabolic and gene regulatory networks modulates the *C. Elegans* dietary response. *Cell* **153**, 253–266. (doi:10.1016/j.cell.2013.02.050)
- Veech RL, Kashiwaya Y, Gates DN, King MT, Clarke K. 2002 The energetics of ion distribution: the origin of the resting electric potential of cells. *IUBMB Life* **54**, 241–252. (doi:10.1080/15216540215678)
- Nuccitelli R. 2003 Endogenous electric fields in embryos during development, regeneration and wound healing. *Radiat. Prot. Dosimetry* **106**, 375–383. (doi:10.1093/oxfordjournals.rpd.a006375)
- Borgens RB. 1988 Voltage gradients and ionic currents in injured and regenerating axons. *Adv. Neurol.* **47**, 51–66.
- McCaig CD, Rajnicek AM, Song B, Zhao M. 2005 Controlling cell behavior electrically: current views and future potential. *Physiol. Rev.* **85**, 943–978. (doi:10.1152/physrev.00020.2004)
- Chifflet S, Hernández JA, Grasso S. 2005 A possible role for membrane depolarization in epithelial wound healing. *Am. J. Physiol. Cell Physiol.* **288**, C1420–C1430. (doi:10.1152/ajpcell.00259.2004)
- Lund EJ. 1924 Experimental control of organic polarity by the electric current. IV. The quantitative relations between current density, orientation, and inhibition of regeneration. *J. Exp. Zool.* **39**, 357–379. (doi:10.1002/jez.1400390208)
- Mathews AP. 1903 Electrical polarity in the hydroids. *Am. J. Physiol.* **8**, 294–299.
- Marsh G, Beams HW. 1952 Electrical control of morphogenesis in regenerating *Dugesia tigrina*. I. Relation of axial polarity to field strength. *J. Cell. Comp. Physiol.* **39**, 191–213. (doi:10.1002/jcp.1030390203)
- Dimmitt J, Marsh G. 1952 Electrical control of morphogenesis in regenerating *Dugesia tigrina*. II. Potential gradient vs. current density as control factors. *J. Cell. Comp. Physiol.* **40**, 11–23. (doi:10.1002/jcp.1030400103)
- Adams DS, Levin M. 2006 Inverse drug screens: a rapid and inexpensive method for implicating molecular targets. *Genesis* **44**, 530–540. (doi:10.1002/dvg.20246)
- Adams DS, Levin M. 2006 Strategies and techniques for investigation of biophysical signals in patterning. In *Analysis of growth factor signaling in embryos* (eds M Whitman, AK Sater), pp. 177–262. London, UK: Taylor and Francis Books.
- Adams DS, Levin M. 2012 Measuring resting membrane potential using the fluorescent voltage reporters DiBAC<sub>4</sub>(3) and CC2-DMPE. *Cold Spring Harb. Protoc.* **2012**, 459–464. (doi:10.1101/pdb.prot067702)
- Adams DS, Tseng AS, Levin M. 2013 Light-activation of the Archaeorhodopsin H<sup>+</sup>-pump reverses age-dependent loss of vertebrate regeneration: sparking system-level controls *in vivo*. *Biol. Open* **2**, 306–313. (doi:10.1242/bio.20133665)
- Adams DS, Lemire JM, Kramer RH, Levin M. 2014 Optogenetics in developmental biology: using light to control ion flux-dependent signals in *Xenopus* embryos. *Int. J. Dev. Biol.* **58**, 851–861. (doi:10.1387/ijdb.140207ml)
- Levin M. 2014 Molecular bioelectricity: how endogenous voltage potentials control cell behavior and instruct pattern regulation *in vivo*. *Mol. Biol. Cell.* **25**, 3835–3850. (doi:10.1091/mbc.E13-12-0708)
- McCaig CD, Song B, Rajnicek AM. 2009 Electrical dimensions in cell science. *J. Cell Sci.* **122**, 4267–4276. (doi:10.1242/jcs.023564)
- Sundelacruz S, Levin M, Kaplan DL. 2009 Role of membrane potential in the regulation of cell proliferation and differentiation. *Stem Cell Rev. Rep.* **5**, 231–246. (doi:10.1007/s12015-009-9080-2)
- Sundelacruz S, Levin M, Kaplan DL. 2008 Membrane potential controls adipogenic and osteogenic differentiation of mesenchymal stem cells. *PLoS ONE* **3**, e3737. (doi:10.1371/journal.pone.0003737)
- Sundelacruz S, Levin M, Kaplan DL. 2015 Comparison of the depolarization response of human mesenchymal stem cells from different donors. *Sci. Rep.* **5**, 18279. (doi:10.1038/srep18279)
- Beane WS, Morokuma J, Adams DS, Levin M. 2011 A chemical genetics approach reveals H,K-ATPase-mediated membrane voltage is required for planarian head regeneration. *Chem. Biol.* **18**, 77–89. (doi:10.1016/j.chembiol.2010.11.012)
- Vandenberg LN, Morrie RD, Adams DS. 2011 V-ATPase-dependent ectodermal voltage and pH regionalization are required for craniofacial morphogenesis. *Dev. Dyn.* **240**, 1889–1904. (doi:10.1002/dvdy.22685)
- Adams DS, Uzel SG, Akagi J, Wlodkovic D, Andreeva V, Yelick PC, Devitt-Lee A, Pare JF, Levin M. 2016 Bioelectric signalling via potassium channels: a mechanism for craniofacial dysmorphogenesis in KCNJ2-associated Andersen-Tawil syndrome. *J. Physiol.* **594**, 3245–3270. (doi:10.1113/JP271930)
- Pai VP, Lemire JM, Pare JF, Lin G, Chen Y, Levin M. 2015 Endogenous gradients of resting potential instructively pattern embryonic neural tissue via notch signalling and regulation of proliferation. *J. Neurosci.* **35**, 4366–4385. (doi:10.1523/JNEUROSCI.1877-14.2015)
- Beane WS, Morokuma J, Lemire JM, Levin M. 2013 Bioelectric signalling regulates head and organ size during planarian regeneration. *Development* **140**, 313–322. (doi:10.1242/dev.086900)

43. Oviedo NJ, Morokuma J, Walentek P, Kema IP, Gu MB, Ahn JM, Hwang JS, Gojobori T, Levin M. 2010 Long-range neural and gap junction protein-mediated cues control polarity during planarian regeneration. *Dev. Biol.* **339**, 188–199. (doi:10.1016/j.ydbio.2009.12.012)
44. Pai VP, Vandenberg LN, Blackiston D, Levin M. 2012 Neurally derived tissues in *Xenopus laevis* embryos exhibit a consistent bioelectrical left-right asymmetry. *Stem Cells Int.* **2012**, 353491. (doi:10.1155/2012/353491)
45. Barghouth PG, Thiruvalluvan M, Oviedo NJ. 2015 Bioelectrical regulation of cell cycle and the planarian model system. *Biochim. Biophys. Acta* **1848**, 2629–2637. (doi:10.1016/j.bbame.2015.02.024)
46. Krüger J, Bohrmann J. 2015 Bioelectric patterning during oogenesis: stage-specific distribution of membrane potentials, intracellular pH and ion-transport mechanisms in *Drosophila* ovarian follicles. *BMC. Dev. Biol.* **15**, 1. (doi:10.1186/s12861-015-0051-3)
47. Emmons-Bell M *et al.* 2015 Gap junctional blockade stochastically induces different species-specific head anatomies in genetically wild-type *Girardia dorotocephala* flatworms. *Int. J. Mol. Sci.* **16**, 27 865–27 896. (doi:10.3390/ijms161126065)
48. Pai VP, Aw S, Shomrat T, Lemire JM, Levin M. 2012 Transmembrane voltage potential controls embryonic eye patterning in *Xenopus laevis*. *Development* **139**, 313–323. (doi:10.1242/dev.073759)
49. Adams DS, Masi A, Levin M. 2007 H<sup>+</sup> pump-dependent changes in membrane voltage are an early mechanism necessary and sufficient to induce *Xenopus* tail regeneration. *Development* **134**, 1323–1335. (doi:10.1242/dev.02812)
50. Tseng AS, Beane WS, Lemire JM, Masi A, Levin M. 2010 Induction of vertebrate regeneration by a transient sodium current. *J. Neurosci.* **30**, 13 192–13 200. (doi:10.1523/JNEUROSCI.3315-10.2010)
51. Chernet BT, Adams DS, Lobikin M, Levin M. 2016 Use of genetically encoded, light-gated ion translocators to control tumorigenesis. *Oncotarget* **7**, 19 575–19 588. (doi:10.18632/oncotarget.8036)
52. Chernet BT, Levin M. 2013 Transmembrane voltage potential is an essential cellular parameter for the detection and control of tumor development in a *Xenopus* model. *Dis. Models Mech.* **6**, 595–607. (doi:10.1242/dmm.010835)
53. Pai VP, Martyniuk CJ, Echeverri K, Sundelacruz S, Kaplan DL, Levin M. 2016 Genome-wide analysis reveals conserved transcriptional responses downstream of resting potential change in *Xenopus* embryos, axolotl regeneration, and human mesenchymal cell differentiation. *Regeneration* **3**, 3–25. (doi:10.1002/reg.2.48)
54. Tseng AS, Carneiro K, Lemire JM, Levin M. 2011 HDAC activity is required during *Xenopus* tail regeneration. *PLoS ONE* **6**, e26382. (doi:10.1371/journal.pone.0026382)
55. Tseng AS, Levin M. 2012 Transducing bioelectric signals into epigenetic pathways during tadpole tail regeneration. *Anat. Rec.* **295**, 1541–1551. (doi:10.1002/ar.22495)
56. Levin M, Stevenson CG. 2012 Regulation of cell behavior and tissue patterning by bioelectrical signals: challenges and opportunities for biomedical engineering. *Annu. Rev. Biomed. Eng.* **14**, 295–323. (doi:10.1146/annurev-bioeng-071811-150114)
57. Lobo D, Levin M. 2015 Inferring regulatory networks from experimental morphological phenotypes: a computational method reverse-engineers planarian regeneration. *PLoS Comput. Biol.* **11**, e1004295. (doi:10.1371/journal.pcbi.1004295)
58. Allen JM, Ross KG, Zayas RM. 2001 Regeneration in invertebrates: model systems. *eLS* 1–9. (doi:10.1002/9780470015902.a0001095.pub2)
59. Almuedo-Castillo M, Sureda-Gómez M, Adell T. 2012 Wnt signalling in planarians: new answers to old questions. *Int. J. Dev. Biol.* **56**, 53–65. (doi:10.1387/ijdb.113451ma)
60. Bayasas JR, Castillo E, Munoz-Marmol AM, Salo E. 1997 Planarian Hox genes: novel patterns of expression during regeneration. *Development* **124**, 141–148.
61. Chen X, Xu C. 2015 Protein expression profiling in head fragments during planarian regeneration after amputation. *Dev. Genes Evol.* **225**, 79–93. (doi:10.1007/s00427-015-0494-3)
62. Werner S, Stückemann T, Beirán Amigo M, Rink JC, Jülicher F, Friedrich BM. 2015 Scaling and regeneration of self-organized patterns. *Phys. Rev. Lett.* **114**, 138101. (doi:10.1103/PhysRevLett.114.138101)
63. Meinhardt H. 2009 Beta-catenin and axis formation in planarians. *BioEssays* **31**, 5–9. (doi:10.1002/bies.080193)
64. Lange CS, Steele VE. 1978 The mechanism of anterior-posterior polarity control in planarians. *Differentiation* **11**, 1–12. (doi:10.1111/j.1432-0436.1978.tb00965.x)
65. Pietak A, Levin M. 2016 Exploring instructive physiological signalling with the bioelectric tissue simulation engine. *Front. Bioeng. Biotechnol.* **4**, 55. (doi:10.3389/fbio.2016.00055)
66. Cervera J, Alcaraz A, Mafe S. 2016 Bioelectrical signals and ion channels in the modelling of multicellular patterns and cancer biophysics. *Sci. Rep.* **6**, 20403. (doi:10.1038/srep20403)
67. Mathews J, Levin M. 2016 Gap junctional signalling in pattern regulation: physiological network connectivity instructs growth and form. *Dev. Neurobiol.* **77**, 643–673. (doi:10.1002/dneu.22405)
68. Makary SM, Claydon TW, Enkvetchakul D, Nichols CG, Boyett MR. 2005 A difference in inward rectification and polyamine block and permeation between the Kir2.1 and Kir3.1/Kir3.4 K<sup>+</sup> channels. *J. Physiol.* **568**, 749–766. (doi:10.1113/jphysiol.2005.085746)
69. Yan DH, Nishimura K, Yoshida K, Nakahira K, Ehara T, Igarashi K, Ishihara K. 2005 Different intracellular polyamine concentrations underlie the difference in the inward rectifier K<sup>+</sup> currents in atria and ventricles of the guinea-pig heart. *J. Physiol.* **563**, 713–724. (doi:10.1113/jphysiol.2004.077677)
70. Haghighi AP, Cooper E. 1998 Neuronal nicotinic acetylcholine receptors are blocked by intracellular spermine in a voltage-dependent manner. *J. Neurosci.* **18**, 4050–4062.
71. Han X *et al.* 2008 Binding of spermine and ifenprodil to a purified, soluble regulatory domain of the N-methyl-D-aspartate receptor. *J. Neurochem.* **107**, 1566–1577. (doi:10.1111/j.1471-4159.2008.05729.x)
72. Kurata HT, Marton LJ, Nichols CG. 2006 The polyamine binding site in inward rectifier K<sup>+</sup> channels. *J. Gen. Physiol.* **127**, 467–480. (doi:10.1085/jgp.200509467)
73. Ifune CK, Steinbach JH. 1991 Voltage-dependent block by magnesium of neuronal nicotinic acetylcholine receptor channels in rat pheochromocytoma cells. *J. Physiol.* **443**, 683–701. (doi:10.1113/jphysiol.1991.sp018858)
74. Horie M, Irisawa H, Noma A. 1987 Voltage-dependent magnesium block of adenosine-triphosphate-sensitive potassium channel in guinea-pig ventricular cells. *J. Physiol.* **387**, 251–272. (doi:10.1113/jphysiol.1987.sp016572)
75. Avery RB, Johnston D. 1996 Multiple channel types contribute to the low-voltage-activated calcium current in hippocampal CA3 pyramidal neurons. *J. Neurosci.* **16**, 5567–5582.
76. Philipson LH, Hice RE, Schaefer K, LaMendola J, Bell GI, Nelson DJ, Steiner DF. 1991 Sequence and functional expression in *Xenopus* oocytes of a human insulinoma and islet potassium channel. *Proc. Natl Acad. Sci. USA* **88**, 53–57. (doi:10.1073/pnas.88.1.53)
77. Harris AL, Spray DC, Bennett MV. 1983 Control of intercellular communication by voltage dependence of gap junctional conductance. *J. Neurosci.* **3**, 79–100.
78. Wright SH. 2004 Generation of resting membrane potential. *AJP: Adv. Physiol. Educ.* **28**, 139–142. (doi:10.1152/advan.00029.2004)
79. Pekař M. 2015 The thermodynamic driving force for kinetics in general and enzyme kinetics in particular. *ChemPhysChem* **16**, 884–885. (doi:10.1002/cphc.201402778)
80. Vrbjar N, Dzurba A, Ziegelhöffer A. 1994 Enzyme kinetics and the activation energy of (Na, K)-ATPase in ischaemic hearts: influence of the duration of ischaemia. *Gen. Physiol. Biophys.* **13**, 405–411.
81. Sachs JR. 1977 Kinetic evaluation of the Na-K pump reaction mechanism. *J. Physiol. (Lond.)* **273**, 489–514. (doi:10.1113/jphysiol.1977.sp012106)
82. Noske R, Cornelius F, Clarke RJ. 2010 Investigation of the enzymatic activity of the Na<sup>+</sup>, K<sup>+</sup>-ATPase via isothermal titration microcalorimetry. *Biochim. Biophys. Acta* **1797**, 1540–1545. (doi:10.1016/j.bbabi.2010.03.021)
83. Lin CH, Lee TH. 2005 Sodium or potassium ions activate different kinetics of Gill Na, K-ATPase in three seawater- and freshwater-acclimated



- euryhaline teleosts. *J. Exp. Zool. A* **303A**, 57–65. (doi:10.1002/jez.a.130)
84. Galli A, Petersen CI. 1997 *Drosophila* serotonin transporters have voltage-dependent uptake coupled to a serotonin-gated ion channel. *J. Neurosci.* **17**, 3401–3411.
  85. Barnes NM, Neumaier JF. 2011 Neuronal 5-HT receptors and SERT. *Trends Biosci. Sci. Rev. Ser.* **34**, 1–16.
  86. Chen L *et al.* 2010 Role of organic cation transporter 3 (SLC22A3) and its missense variants in the pharmacologic action of metformin. *Pharmacogenet. Genomics* **20**, 687–699. (doi:10.1097/FPC.0b013e32833fe789)
  87. Kekuda R, Prasad PD, Wu X, Wang H, Fei YJ, Leibach FH, Ganapathy V. 1998 Cloning and functional characterization of a potential-sensitive, polyspecific organic cation transporter (OCT3) most abundantly expressed in placenta. *J. Biol. Chem.* **273**, 15 971–15 979. (doi:10.1074/jbc.273.26.15971)
  88. Wessler I, Roth E, Deutsch C, Brockerhoff P, Bittinger F, Kirkpatrick CJ, Kilbinger H. 2001 Release of non-neuronal acetylcholine from the isolated human placenta is mediated by organic cation transporters. *Br. J. Pharmacol.* **134**, 951–956. (doi:10.1038/sj.bjp.0704335)
  89. Wu X, Kekuda R, Huang W, Fei YJ, Leibach FH, Chen J, Conway SJ, Ganapathy V. 1998 Identity of the organic cation transporter OCT3 as the extraneuronal monoamine transporter (Uptake2) and evidence for the expression of the transporter in the brain. *J. Biol. Chem.* **273**, 32776–32786. (doi:10.1074/jbc.273.49.32776)
  90. Mackenzie B, Ujwal ML, Chang MH, Romero MF, Hediger MA. 2006 Divalent metal-ion transporter DMT1 mediates both  $H^{+}$ -coupled  $Fe^{2+}$  transport and uncoupled fluxes. *Pflügers Archiv. Eur. J. Physiol.* **451**, 544–558. (doi:10.1007/s00424-005-1494-3)
  91. Skjærringe T, Burkhart A, Johnsen KB, Moos T. 2015 Divalent metal transporter 1 (DMT1) in the brain: implications for a role in iron transport at the blood-brain barrier, and neuronal and glial pathology. *Front. Mol. Neurosci.* **8**, 19. (doi:10.3389/fnmol.2015.00019)
  92. Chong WS. 2005 Expression of divalent metal transporter 1 (DMT1) isoforms in first trimester human placenta and embryonic tissues. *Hum. Reprod.* **20**, 3532–3538. (doi:10.1093/humrep/dei246)
  93. Talley EM, Sirois JE, Lei Q, Bayliss DA. 2003 Two-pore-domain (Kcnk) potassium channels: dynamic roles in neuronal function. *Neuroscientist* **9**, 46–56. (doi:10.1177/1073858402239590)
  94. Miki T, Nagashima K, Seino S. 1999 The structure and function of the ATP-sensitive  $K^{+}$  channel in insulin-secreting pancreatic beta-cells. *J. Mol. Endocrinol.* **22**, 113–123. (doi:10.1677/jme.0.0220113)
  95. Craig TJ, Ashcroft FM, Proks P. 2008 How ATP inhibits the open  $K_{ATP}$  channel. *J. Gen. Physiol.* **132**, 131–144. (doi:10.1085/jgp.200709874)
  96. Morris KA. 2011 What is hysteresis? *Appl. Mech. Rev.* **64**, 050801. (doi:10.1115/1.4007112)
  97. Gruss M, Mathie A, Lieb WR, Franks NP. 2004 The two-pore-domain  $K^{+}$  channels TREK-1 and TASK-3 are differentially modulated by copper and zinc. *Mol. Pharmacol.* **66**, 530–537.
  98. Ishihara K. 1997 Time-dependent outward currents through the inward rectifier potassium channel IRK1. *J. Gen. Physiol.* **109**, 229–243. (doi:10.1085/jgp.109.2.229)
  99. McKay MC, Worley JF. 2001 Linoleic acid both enhances activation and blocks Kv1.5 and Kv2.1 channels by two separate mechanisms. *Am. J. Physiol. Cell Physiol.* **281**, C1277–C1284.
  100. Morgan TH, Dimon AC. 1904 An examination of the problems of physiological 'polarity' and of electrical polarity in the earthworm. *J. Exp. Zool.* **1**, 331–347. (doi:10.1002/jez.1400010206)
  101. Sater AK. 2011 A jump-start for planarian head regeneration. *Chem. Biol.* **18**, 4–5. (doi:10.1016/j.chembiol.2011.01.002)
  102. Lobo D, Beane WS, Levin M. 2012 Modeling planarian regeneration: a primer for reverse-engineering the worm. *PLoS Comput. Biol.* **8**, e1002481. (doi:10.1371/journal.pcbi.1002481)
  103. Gentile L, Cebrià F, Bartscherer K. 2011 The planarian flatworm: an *in vivo* model for stem cell biology and nervous system regeneration. *Dis. Models Mech.* **4**, 12–19. (doi:10.1242/dmm.006692)
  104. Durant F, Lobo D, Hammelman J, Levin M. 2016 Physiological controls of large-scale patterning in planarian regeneration: a molecular and computational perspective on growth and form: physiological controls of anatomy. *Regeneration* **3**, 78–102. (doi:10.1002/reg2.54)
  105. Adell T, Cebrià F, Salo E. 2010 Gradients in planarian regeneration and homeostasis. *Cold Spring Harb. Perspect. Biol.* **2**, a000505. (doi:10.1101/cshperspect.a000505)
  106. Oviedo NJ, Levin M. 2007 Smedinx-11 is a planarian stem cell gap junction gene required for regeneration and homeostasis. *Development* **134**, 3121–3131. (doi:10.1242/dev.006635)
  107. Maricq AV, Peterson AS, Brake AJ, Myers RM, Julius D. 1991 Primary structure and functional expression of the 5HT3 receptor, a serotonin-gated ion channel. *Science* **254**, 432–437. (doi:10.1126/science.1718042)
  108. Torráo AS, Britto LRG. 2002 Neurotransmitter regulation of neural development: acetylcholine and nicotinic receptors. *An. Acad. Bras. Ciênc.* **74**, 453–461. (doi:10.1590/S0001-37652002003000008)
  109. Blanke ML, VanDongen AMJ. 2009 Activation mechanisms of the NMDA receptor. In *Biology of the NMDA receptor* (ed. AM Van Dongen), pp. 283–312. Boca Raton, FL: CRC Press.
  110. Zhao X, Yeh JZ, Salgado VL, Narahashi T. 2004 Fipronil is a potent open channel blocker of glutamate-activated chloride channels in cockroach neurons. *J. Pharmacol. Exp. Ther.* **310**, 192–201. (doi:10.1124/jpet.104.065516)
  111. Geng Y, Magleby KL. 2015 Single-channel kinetics of BK (Slo1) channels. *Front. Physiol.* **5**, 532. (doi:10.3389/fphys.2014.00532)
  112. Noam Y, Wadman WJ. 2008 On the voltage-dependent  $Ca^{2+}$  block of serotonin 5-HT3 receptors: a critical role of intracellular phosphates. *J. Physiol.* **586**, 3629–3638. (doi:10.1113/jphysiol.2008.153486)
  113. Kirson ED, Schirra C, Konnerth A, Yaari Y. 1999 Early postnatal switch in magnesium sensitivity of NMDA receptors in rat CA1 pyramidal cells. *J. Physiol.* **521**, 99–111. (doi:10.1111/j.1469-7793.1999.00099.x)
  114. Noh S, Lee SR, Jeong YJ, Ko KS, Rhee BD, Kim N, Han J. 2015 The direct modulatory activity of zinc toward ion channels. *Integr. Med. Res.* **4**, 142–146. (doi:10.1016/j.imr.2015.07.004)
  115. Ashcroft FM. 2005 ATP-sensitive potassium channelopathies: focus on insulin secretion. *J. Clin. Investig.* **115**, 2047–2058. (doi:10.1172/JCI25495)
  116. Tang XD, Santarelli LC, Hoshi T. 2004 Metabolic regulation of potassium channels. *Annu. Rev. Physiol.* **66**, 131–159. (doi:10.1146/annurev.physiol.66.041002.142720)
  117. Willert K, Nusse R. 2012 Wnt proteins. *Cold Spring Harb. Perspect. Biol.* **4**, a007864. (doi:10.1101/cshperspect.a007864)
  118. Stolor MA, Shi YB. 1995 *Xenopus* sonic hedgehog as a potential morphogen during embryogenesis and thyroid hormone-dependent metamorphosis. *Nucleic Acids Res.* **23**, 2555–2562. (doi:10.1093/nar/23.13.2555)
  119. Taylor JM, Mitchell WM, Cohen S. 1972 Epidermal growth factor physical and chemical properties. *J. Biol. Chem.* **247**, 5928–5934.
  120. Gospodarowicz D, Ferrara N, Schweigerer L, Neufeld G. 1987 Structural characterization and biological functions of fibroblast growth factor. *Endocr. Rev.* **8**, 95–114. (doi:10.1210/edrv-8-2-95)
  121. Adams DS, Levin M. 2012 General principles for measuring resting membrane potential and ion concentration using fluorescent bioelectricity reporters. *Cold Spring Harb. Protoc.* **2012**, 385–397. (doi:10.1101/pdb.top067710)
  122. Costa PF, Emilio MG, Fernandes PL, Ferreira HG, Ferreira KG. 1989 Determination of ionic permeability coefficients of the plasma membrane of *Xenopus laevis* oocytes under voltage clamp. *J. Physiol. (Lond.)* **413**, 199–211. (doi:10.1113/jphysiol.1989.sp017649)
  123. Rose EM, Koo JCP, Antkoff JE, Ahmed SM, Angers S, Hampson DR. 2009 Glutamate transporter coupling to  $Na,K$ -ATPase. *J. Neurosci.* **29**, 8143–8155. (doi:10.1523/JNEUROSCI.1081-09.2009)
  124. Blackiston D, Adams DS, Lemire JM, Lobikin M, Levin M. 2011 Transmembrane potential of GlyCl-expressing instructor cells induces a neoplastic-like conversion of melanocytes via a serotonergic pathway. *Dis. Models Mech.* **4**, 67–85. (doi:10.1242/dmm.005561)

125. Tanaka EM, Reddien PW. 2011 The cellular basis for animal regeneration. *Dev. Cell.* **21**, 172–185. (doi:10.1016/j.devcel.2011.06.016)
126. Cooke J. 1981 Scale of body pattern adjusts to available cell number in amphibian embryos. *Nature* **290**, 775–778. (doi:10.1038/290775a0)
127. Tam PPL, Rossant J. 2003 Mouse embryonic chimeras: tools for studying mammalian development. *Development* **130**, 6155–6163. (doi:10.1242/dev.00893)
128. Perathoner S, Daane JM, Henrion U, Seeböhm G, Higdon CW, Johnson SL, Nüsslein-Volhard C, Harris MP. 2014 Bioelectric signaling regulates size in zebrafish fins. *PLoS Genet.* **10**, e1004080. (doi:10.1371/journal.pgen.1004080)
129. Litan A, Langhans SA. 2015 Cancer as a channelopathy: ion channels and pumps in tumor development and progression. *Front. Cell. Neurosci.* **9**, 86. (doi:10.3389/fncel.2015.00086)
130. Veale EL, Hassan M, Walsh Y, Al-Moubarak E, Mathie A. 2014 Recovery of current through mutated TASK3 potassium channels underlying Birk Barel syndrome. *Mol. Pharmacol.* **85**, 397–407. (doi:10.1124/mol.113.090530)
131. Kortüm F *et al.* 2015 Mutations in KCNH1 and ATP6V1B2 cause Zimmermann-Laband syndrome. *Nat. Genet.* **47**, 661–667. (doi:10.1038/ng.3282)
132. Masotti A *et al.* 2015 Keppen-Lubinsky syndrome is caused by mutations in the inwardly rectifying  $K^+$  channel encoded by KCNJ6. *Am. J. Hum. Genet.* **96**, 295–300. (doi:10.1016/j.ajhg.2014.12.011)
133. Skarsfeldt MA, Carstensen H, Skibsbjerg L, Tang C, Buhl R, Bentzen BH, Jespersen T. 2016 Pharmacological inhibition of  $I_K^1$  by PA-6 in isolated rat hearts affects ventricular repolarization and refractoriness. *Physiol. Rep.* **4**, e12734. (doi:10.14814/phy2.12734)
134. Sim JH, Yang DK, Kim YC, Park SJ, Kang TM, So I, Kim KW. 2002 ATP-sensitive  $K^+$  channels composed of Kir6.1 and SUR2B subunits in guinea pig gastric myocytes. *Am. J. Physiol. Gastrointest. Liver Physiol.* **282**, G137–G144. (doi:10.1152/ajpgi.00057.2002)
135. Aw S, Koster JC, Pearson W, Nichols CG, Shi NQ, Carneiro K, Levin M. 2010 The ATP-sensitive  $K^+$ -channel (KATP) controls early left–right patterning in *Xenopus* and chick embryos. *Dev. Biol.* **346**, 39–53. (doi:10.1016/j.ydbio.2010.07.011)
136. Lobo D, Solano M, Bubenik GA, Levin M. 2014 A linear-encoding model explains the variability of the target morphology in regeneration. *J. R. Soc. Interface* **11**, 20130918. (doi:10.1098/rsif.2013.0918)
137. Salo E *et al.* 2009 Planarian regeneration: achievements and future directions after 20 years of research. *Int. J. Dev. Biol.* **53**, 1317–1327. (doi:10.1387/ijdb.072414es)
138. Schiffmann Y. 1991 An hypothesis: phosphorylation fields as the source of positional information and cell differentiation—(cAMP, ATP) as the universal morphogenetic turing couple. *Prog. Biophys. Mol. Biol.* **56**, 79–105. (doi:10.1016/0079-6107(91)90015-K)
139. Nogi T, Levin M. 2005 Characterization of *Innexin* gene expression and functional roles of gap-junctional communication in planarian regeneration. *Dev. Biol.* **287**, 314–335. (doi:10.1016/j.ydbio.2005.09.002)
140. Fukumoto T, Kema I, Levin M. 2005 Serotonin signaling is a very early step in patterning of the left-right axis in chick and frog embryos. *Curr. Biol.* **15**, 794–803. (doi:10.1016/j.cub.2005.03.044)
141. Vandenberg LN, Blackiston DJ, Rea AC, Dore TM, Levin M. 2014 Left-right patterning in *Xenopus* conjoined twin embryos requires serotonin signaling and gap junctions. *Int. J. Dev. Biol.* **58**, 799–809. (doi:10.1387/ijdb.140215ml)
142. Esser AT, Smith KC, Weaver JC, Levin M. 2006 Mathematical model of morphogen electrophoresis through gap junctions. *Dev. Dyn.* **235**, 2144–2159. (doi:10.1002/dvdy.20870)
143. Cooper MS, Miller JP, Fraser SE. 1989 Electrophoretic repatterning of charged cytoplasmic molecules within tissues coupled by gap junctions by externally applied electric fields. *Dev. Biol.* **132**, 179–188. (doi:10.1016/0012-1606(89)90216-9)
144. Jansson B. 1989 Dietary, total body, and intracellular potassium-to-sodium ratios and their influence on cancer. *Cancer Detect. Prev.* **14**, 563–565.
145. Jansson B. 1996 Potassium, sodium, and cancer: a review. *J. Environ. Pathol. Toxicol. Oncol.* **15**, 65–73.
146. Bates E. 2015 Ion channels in development and cancer. *Annu. Rev. Cell. Dev. Biol.* **31**, 231–247. (doi:10.1146/annurev-cellbio-100814-125338)
147. Doan TN, Stephans K, Ramirez AN, Glazebrook PA, Andresen MC, Kunze DL. 2004 Differential distribution and function of hyperpolarization-activated channels in sensory neurons and mechanosensitive fibers. *J. Neurosci.* **24**, 3335–3343. (doi:10.1523/JNEUROSCI.5156-03.2004)
148. Long X, Ye J, Zhao D, Zhang SJ. 2015 Magnetogenetics: remote non-invasive magnetic activation of neuronal activity with a magnetoreceptor. *Sci. Bull.* **60**, 2107–2119. (doi:10.1007/s11434-015-0902-0)
149. Kastrop CJ, Runyon MK, Lucchetta EM, Price JM, Ismagilov RF. 2008 Using chemistry and microfluidics to understand the spatial dynamics of complex biological networks. *Acc. Chem. Res.* **41**, 549–558. (doi:10.1021/ar700174g)
150. Cervera J, Manzanares JA, Mafe S. 2015 Electrical coupling in ensembles of nonexcitable cells: modeling the spatial map of single cell potentials. *J. Phys. Chem. B* **119**, 2968–2978. (doi:10.1021/jp512900x)
151. Cervera J, Alcaraz A, Mafe S. 2014 Membrane potential bistability in nonexcitable cells as described by inward and outward voltage-gated ion channels. *J. Phys. Chem. B* **118**, 12 444–12 450. (doi:10.1021/jp508304h)
152. Hoel EP, Albantakis L, Tononi G. 2013 Quantifying causal emergence shows that macro can beat micro. *Proc. Natl Acad. Sci. USA* **110**, 19 790–19 795. (doi:10.1073/pnas.1314922110)